

# Seismic tremor location of 10 large paroxysmal eruptions of Tungurahua volcano, Ecuador

Pablo B. Palacios<sup>1</sup>,<sup>2</sup> Heidy M. Mader,<sup>2</sup> J.-Michael Kendall<sup>3</sup> and Hugo A. Yepes<sup>1,4</sup>

<sup>1</sup>Geophysical Institute, National Polytechnic School, Quito 170525, Ecuador. E-mail: [ppalacios@igepn.edu.ec](mailto:ppalacios@igepn.edu.ec)

<sup>2</sup>School of Earth Sciences, University of Bristol, Bristol BS8 1TL, UK

<sup>3</sup>Department of Earth Sciences, University of Oxford, Oxford OX1 2JD, UK

<sup>4</sup>Risk Advisor for the Mayor's Office, Municipality of Quito, Ecuador

Accepted 2022 December 19. Received 2022 October 27; in original form 2022 June 8

## SUMMARY

The most recent eruptive period of Tungurahua volcano lasted 17 yr (1999–2016), generating strong eruptive phases with the release of large amounts of seismic and acoustic energies. We have selected 10 large eruptions and located their seismic sources. The location method involves applying a new method for correcting for site effects in the seismic records and identifying, in the frequency domain, the signals from the ground-coupled airwaves and pyroclastic flows. The locations are computed by minimizing the differences of the source energy rates in the [0.4, 2.5] Hz range. The results suggest that the first three eruptions have locations mainly concentrated at the [−1, 2] km depth range (asl), and the locations of the fourth eruption are mainly coincident with depths of a possible reservoir estimated from petrological studies. This fact strongly suggests that this eruption was responsible of changes in the dynamics of Tungurahua, making the volcano prone to produce Vulcanian eruptions.

**Key words:** Volcano seismology; Seismic noise; Site effects; Explosive volcanism.

## 1 INTRODUCTION

Paroxysmal eruptions mark the most dangerous stage of an eruptive cycle, where the volcanic crater is open and able to produce violent ash explosions and pyroclastic flows. However, not all paroxysmal events are the same—they vary widely in intensity and with degrees of precursory activity, varying from none to protracted (Giordano & De Astis 2021). Furthermore, petrologic studies of eruptive magma indicate the style of eruption is linked to the composition, depth and genesis of magma, potentially from more than one reservoir (Pappalardo *et al.* 2014). Geophysical signals (e.g. seismic) may offer insights into these variations in eruptive style. Here, we investigate seismic activity and acoustic signals during 10 paroxysmal eruptions of Tungurahua volcano.

Tungurahua is an andesitic stratovolcano located in the Eastern Cordillera of Ecuador (latitude −1.47, longitude −78.45), and is one of the more active volcanoes in the Northern Andes (Hall *et al.* 1999; Le Pennec *et al.* 2008; Bablon *et al.* 2018). Its latest eruptive period lasted 17 yr, from 1999 to 2016. To mitigate the hazard in the region, a monitoring system was installed since 1989 (Le Pennec 2005), maintained and improved (Kumagai *et al.* 2007) over the years by the IGEPN (Geophysical Institute of the National Polytechnic School—Quito) together with international support and collaboration. Data emerging from this system have motivated several seismic and acoustic studies (Molina 2001; Johnson *et al.* 2003; Molina *et al.* 2005; De la Cruz-Reyna *et al.* 2010; Fee *et al.* 2010;

Kumagai *et al.* 2011b; Kim *et al.* 2014; Kumagai *et al.* 2015; Palacios *et al.* 2016; Bell *et al.* 2017; Anderson *et al.* 2018; Battaglia *et al.* 2019).

The dynamics of Tungurahua can be split into three main periods after its eruption in 1999 October. In the first, 1999 October–2005 December, the volcano produced Strombolian eruptions and ash emissions of variable intensity (Le Pennec 2005), being the strongest in 2001 August. This type of activity included also the generation of short-lived explosions (with records lasting few tens of seconds), long periods (LP) events, and scarce volcano tectonic (VT) earthquakes, all of them declining during the last months of 2005. The second period, 2006 January–2010 May, started with stronger and deeper LPs, more frequent tremors and explosions, setting a clear increase in 2006 May, compared with previous daily numbers of events. Then, on 2006 July 14 a sustained eruption occurred (VEI 2), generating the first pyroclastic flows. A month later, on August 16, the strongest eruption (VEI 3) produced extensive pyroclastic flows with effects mainly on the flanks from the north–west to south–west. These two eruptions were preceded by several days with hundreds of explosions per day, at levels no recorded before them. Both cases can be considered as Subplinian eruptions. A third important eruption occurred on 2008 February 6 (VEI 2). This case produced pyroclastic flows and was also preceded by several days with hundreds of explosions, being sustained enough to be considered as Subplinian case and very similar to the eruption on 2006 July 14 (IGEPN 2008). Other minor eruptions occurred up to 2010

May. The third period, 2010 May–2016 March, starts with a strong and unmistakable Vulcanian eruption on 2010 May 28 (Bustillos 2010), which generated pyroclastic flows almost immediately after its onset. In this last period, other Vulcanian eruptions, producing pyroclastic flows, were recorded on 2012 December 16, 2013 July 14 and 2014 February (Hall *et al.* 2015; Gaunt *et al.* 2020). This period ends with a sustained eruption on 2016 February 26, preceded by several strong explosions with significant ash emissions (IGEPN 2016). After these eruptions, other minor eruptive events occurred during the next months, but declining in the number and intensity of them. After 2016, it remains only the generation of small VT earthquakes, at a rate  $<2$  events per day, and it is currently considered that the volcano actually finished its eruptive sequence and started a new long repose period.

To better understand the dynamics changes of Tungurahua volcano, and to integrate the seismic and acoustic knowledge of it, we require precise seismic source locations of its large eruptions, which is the main goal of this paper. Large eruptions, here called paroxysms, cause large amounts of seismic and acoustic energies, including those from pyroclastic flows, which generate high-frequency seismic waves when they strike the ground, and ground-coupled airwaves from jets and forced plumes formed during the entrainment of tephra and gases into the atmosphere. Eventually, the effect of these phenomena on the records is here considered and the seismic body waves of the tremors are separated from the main signal. Precise locations are then computed.

Our approach is based on far-field approximations (Madariaga 2015) of the energy rate released by the seismic sources, which are computed from wave amplitudes. Therefore, we must first correct for site effects (Campillo *et al.* 1989; Semblat *et al.* 2005; Cruz-Atienza *et al.* 2016) in the measured amplitudes. Site effects are caused by the interaction of seismic waves with local geological structures around the seismic stations. They arise because of constructive and destructive seismic wave interference and changes in the velocity field (Yoshida 2015), and also due to scattering and backscattering processes of seismic waves (Aki 1969; Sato *et al.* 2012). For such corrections, we here generalize the method proposed by Palacios *et al.* (2015), which is based on seismic noise properties, and provide a theoretical background to explain it.

Our second task is to identify the air-to-ground coupling of airwaves (Ben-Menahem & Singh 2000; Ichihara *et al.* 2021). This is done in the frequency range by computing the Fourier transform of the cross-correlation between infrasound and the seismic waves, which is called coherence (Buttkus 2000; Sciotto *et al.* 2011; Palacios *et al.* 2016). We use the squared amplitude of this coherence and select those ranges where it is null or weak in order to eliminate the effect of the airwaves on the seismic records.

To locate the eruptive tremor, we take into account refractions of seismic waves within the volcanic edifice, which is done by using the velocity model obtained using the 3D tomography (Molina *et al.* 2005). Finally, the source location depths are used to interpret and compare them with petrological studies (Samaniego *et al.* 2011; Hall *et al.* 2015; Andújar *et al.* 2017) for the Tungurahua volcano.

## 2 METHODS

### 2.1 Data

We use seismic data recorded by six broad-band sensors (BRUN, BMAS1, BCUS, BBIL, BMAS and BPAT), which were installed on Tungurahua volcano flanks between 2006 July and 2009 April

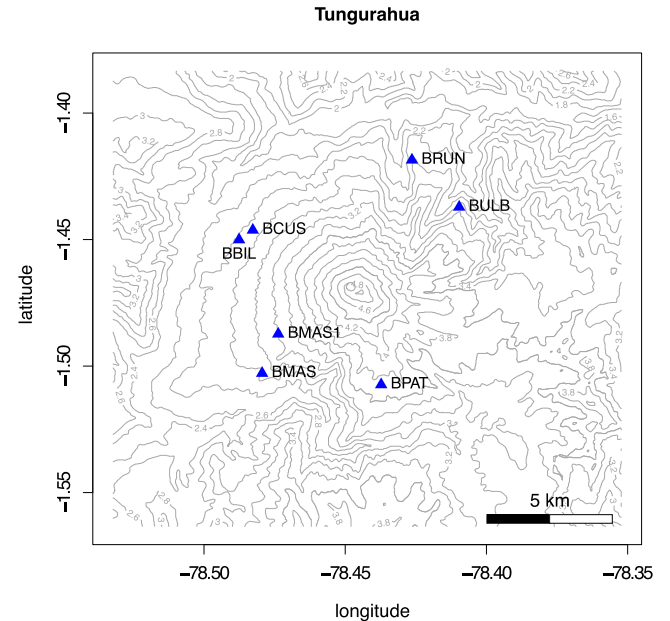


**Figure 1.** Broad-band seismo-acoustic stations of JICA project on Tungurahua volcano, installed between 2006 and 2009.

**Table 1.** Ten large eruptions of Tungurahua between 2006 and 2016.

Ex	Date–time onset	Duration (h)	Stations used
E1	20060714–22:40	4.2	BCUS, BMAS1, BRUN
E2	20060816–14:00	16.3	BCUS, BMAS1, BRUN
E3	20080206–04:15	9.6 <sup>(1,2)</sup>	BMAS, BPAT, BRUN
E4	20100528–14:00	3.7	BBIL, BMAS, BPAT, BRUN
E5	20101204–13:55	4.5 <sup>(1)</sup>	BBIL, BMAS, BPAT, BRUN
E6	20120204–10:50	3.4 <sup>(1)</sup>	BBIL, BMAS, BPAT, BRUN
E7	20121216–12:34	8.1 <sup>(1)</sup>	BBIL, BMAS, BPAT, BRUN
E8	20130714–11:45	1.2	BBIL, BMAS, BPAT, BRUN
E9	20140201–22:38	5.9	BBIL, BMAS, BPAT, BRUN
E10	20160226–18:32	4.0	BBIL, BMAS, BPAT, BRUN

<sup>(1)</sup>The paroxysm is actually formed by two seismic pulses.

<sup>(2)</sup>The records permit to locate only the first pulse – 4.2 h.

(Fig. 1). The first three stations recorded the first two paroxysms in July and August 2006. During the August eruption, BCUS and BMAS1 were partially destroyed. This circumstance limits the length of the collected seismic noise and also the number of earthquakes that can be used in this study. A seventh existing station has been excluded because high coherence between seismic noise and infrasound records was found. All the stations include a CMG-40T Guralp seismometer, an infrasonic microphone ACO type 7144 and a Smart-24D digitiser. All time series are sampled at 50 Hz. For BCUS and BMAS1 stations, we use the same 4-h noise sample and five earthquakes described in Palacios *et al.* (2015). For the other stations, we use 24-h samples of seismic noise and an additional 36 earthquakes recorded by the stations, giving a set of 41 earthquakes (Appendix A). The earthquakes belong to the period 2006 Jul 28–2014 August 12, most between 100 and 300 km epicentral distance respect to the volcano, with magnitudes larger than 3.7 MLv. Each earthquake is recorded by all the stations, and exhibits a high signal-to-noise ratio. They are chosen when the volcano activity was null or weak, and when any teleseismic event was not recorded.

We focus our analysis on 10 paroxysmal eruptions, E1–E10, listed in Table 1 in chronological order, from 2006 July –2016

February, and shown in Fig. 2. All of them were large enough to produce pyroclastic flows, and at the time warnings for authorities and in-habitants were issued by the IGEPN. These paroxysms are considered as VEI 2 eruptions with E2 as an exception (VEI 3).

## 2.2 Site effect corrections

We need to corrected for seismic site effects before applying any location method based on seismic amplitudes (Kumagai *et al.* 2010). Palacios *et al.* (2015) propose to compute these effects by the normalization of the seismic-noise amplitude spectra at each station. In that normalization, the reference levels are computed to discriminate those frequencies amplified by the site from those attenuated. The reference levels are given by constants, which depend only on the station and component and are the same across the entire frequency band. In this section, we generalize the normalization process by letting the reference levels be frequency functions.

The site frequency response function (FRF), also known as site transfer function, should satisfy the following physical properties:

Property 1: Higher frequency seismic waves must have attenuation factors ( $<1$ ) that decrease with increasing frequencies. This occurs because of heterogeneous media scatter waves whose wavelengths are smaller or similar to the correlation distance of the heterogeneity (Sato *et al.* 2012).

Property 2: Very long-period seismic waves arriving to a site should not be strongly modified, basically because they are not able to interact with the site structures (Sato *et al.* 2012). Initially, we would propose a factor of 1 for the response of these waves. However, if our sensors are installed at the surface, as is the case at Tungurahua volcano, we need to correct it because, when a wave arrives at a free-boundary surface, part of the energy is reflected, but the displacement at the surface can be as much as duplicated if the incident wave is vertical. In general, the factor must be between 1 and 2, depending on the incident angle. Note that waves from distant and deep earthquakes tend to arrive with low incident angles, that is, nearly vertical (Yoshida 2015).

Property 3: FRFs are expected to behave smoothly in the frequency domain. This continuity condition implies that the complexity and disorder of the natural ground will not produce almost monochromatic resonant spikes or thin absorption bands. That might occur, for example, when the responding system is isolated and embedded in a quasi-homogenous medium, such as the response of atoms or molecules in an empty space to incident sunlight.

Property 4: FRFs must be the same, independent of the record type: displacement, velocity or acceleration. This invariance comes from the fact that the site response depends only on ground properties, which we assume are not changing in time. It follows that the ground response to incoming waves must be independent of how that response is measured.

Property 5: Because the sites are formed from layers, whose horizontal dimensions are larger than the vertical, like the case of basins, amplitude differences between vertical and horizontal components arise in the records, which depend on both the impedance contrasts between layers, and their geological geometry. The latter is responsible in some cases for constructive interferences. Therefore, correction of the seismic records for the site effect should result in more similarity between the horizontal and vertical components at each seismic station.

For the determination of the FRFs, we compare the records of distant earthquakes in a group of stations relatively close between them, such those installed on the Tungurahua volcano flanks. Let  $F_{ijk}(f)$  be the component  $k$  (Z, N, E; vertical, north and east) of the FRF at the station  $i$ , as a function of the frequency  $f$ .

Then, if  $l_{ik}(f)$  is the corresponding normalization level function, we define

$$F_{ijk}(f) = \frac{N_{ijk}(f)}{l_{ik}(f)}, \quad (1)$$

being  $l_{ik}(f) > 0$  and  $N_{ijk}(f)$  the amplitude of the seismic noise spectrum. The normalization levels have the same physical units than the noise, generating dimensionless FRFs.

If  $\tilde{A}_{ijk}(f)$  is the spectral amplitude of a distant earthquake recorded at the station  $i$ , then its amplitude with site effect correction is

$$A_{ijk}(f) = \frac{\tilde{A}_{ijk}(f)}{F_{ijk}(f)} = l_{ik}(f) \frac{\tilde{A}_{ijk}(f)}{N_{ijk}(f)} = l_{ik}(f) R_{ijk}(f), \quad (2)$$

after using eq. (1). This expression shows that the site correction depends essentially on the signal-to-noise ratio  $R_{ijk}(f)$ , which is interpreted as an expression that cancel out the site effect information, because both earthquake and seismic noise waves cross the same local structures.

We estimate the portion of the energy density  $E_{ijk}(f) df$  released by the earthquake, around a thin frequency band  $df$ , as a quantity proportional to the squared site-corrected velocities (assuming here that the records have velocity units),

$$\begin{aligned} E_{ijk}(f) df &= \alpha(\bar{r}) P_{ijk}(f) A_{ijk}^2(f) df \\ &= \alpha(\bar{r}) P_{ijk}(f) l_{ik}^2(f) R_{ijk}^2(f) df, \end{aligned} \quad (3)$$

where  $P_{ijk}(f)$  is the factor needed to take into account the source radiation pattern effect and the non-elastic attenuation in the source-station path, while  $\alpha(\bar{r})$  is a factor that account for the elastic attenuation depending only on the reduced distance  $\bar{r}$ , which is the average of all source-station hypocentral distances  $r_i$ . This is equivalent to relocate each station at the same hypocentral distance  $\bar{r}$ , while the amplitudes are corrected by the factor  $r_i/\bar{r}$ . Consequently, the spectrum  $\tilde{A}_{ijk}(f)$  is actually the Fourier Transform amplitude of the product between the recorded time-series and the factor  $r_i/\bar{r}$ .

Because we are considering a distant earthquake, the path and the source rupture mechanism effects will have similar influence on all stations for any frequency  $f$ , that is,  $P_{ijk}(f) = P_k(f)$ . Then, if we select a second station  $j$ , the source energy density estimation  $E_{jlk}(f) df$  should be similar to that found with the station  $i$ , that is, the difference between these energies should be minimum. Therefore, the following residual, which take into account all the station pairs, from a set of  $n$  stations,

$$\begin{aligned} \mathcal{R}(f) &= \sum_{i>j} (E_{ijk}(f) - E_{jlk}(f))^2 \\ &= \frac{1}{2} \sum_{i,j=1}^n (E_{ijk}(f) - E_{jlk}(f))^2, \end{aligned} \quad (4)$$

must be minimum selecting the right reference levels. Writing this residual as function of the normalization levels, using the eq. (3), it gets the form

$$\mathcal{R}(f) = \frac{\alpha(\bar{r})}{2} P_k(f) df \sum_{i,j=1}^n (l_{ik}^2(f) R_{ijk}^2(f) - l_{jk}^2(f) R_{jlk}^2(f))^2, \quad (5)$$

where the factors in front of the sums are common to all the stations. Then, it is enough to find the reference levels that minimize the function

$$\Delta_k(f) = \sum_{i,j=1}^n (l_{ik}^2(f) R_{ijk}^2(f) - l_{jk}^2(f) R_{jlk}^2(f))^2, \quad (6)$$

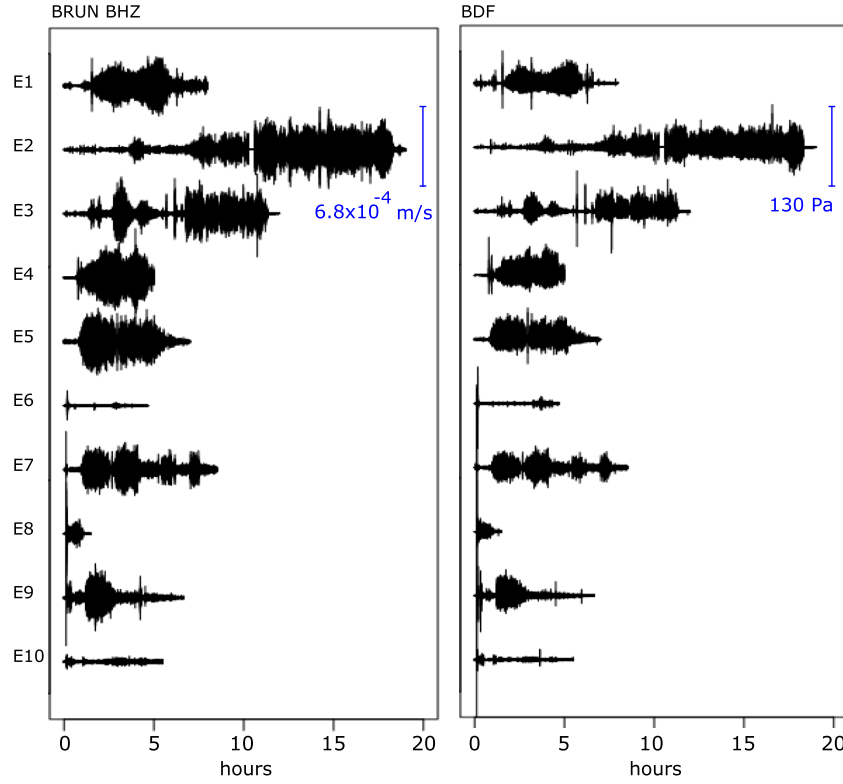


**Figure 2.** Row data, filtered below 5 Hz, of vertical (BHZ— $\text{m s}^{-1}$ ) and infrasound (BDF—Pa) components at BRUN station of all the paroxysms.

in order to get the site response at the frequency  $f$ .

Let us consider the vector  $I_k(f) = (I_{1|k}(f), \dots, I_{n|k}(f))$  as an element of the  $n$ -dimensional Euclidean vectorial space  $\Lambda$ . The null vector  $I_k(f) = \mathbf{0}$  is the global and trivial solution that just generates the minimum residual  $\Delta_k(f) = 0$ . But this result is not physically possible because it causes FRFs with infinite amplitudes. To get a unique FRF with finite amplitudes at each site and component, it is needed to provide some additional constraint.

Because it is expected that a site causes small amplitude changes to very low-frequency waves (Property 2), we define the following boundary condition in the frequency domain for the FRF,

$$\lim_{f \rightarrow 0^+} F_{i|k}(f) = \lim_{f \rightarrow 0^+} \frac{N_{i|k}(f)}{I_{i|k}(f)} = 2. \quad (7)$$

Theoretically, if the noise is stationary and its trend is removed, its Fourier Transform goes to zero at frequency zero (Buttkus 2000). Then, in order to have a finite value in the previous limit, the same behaviour must have the normalization levels, showing an indetermination form  $0/0$  within the limit. For this reason, we follow the next approximation:

$$I_k(0) \approx \frac{1}{2} (N_{1|k}(\epsilon), \dots, N_{n|k}(\epsilon)), \quad (8)$$

being  $\epsilon$  the smaller positive frequency value that we are measuring. This approximation implies that  $F_{i|k}(0) = 2$  for all station  $i$ , and also that low-frequency waves arrive with low incident angles. It is justified due to the refraction of body waves of distant earthquakes travel from high-velocity media (crust) to low-velocity media (volcanic regions), therefore, arriving with low incident angles.

Now, suppose we know that for  $f_0$ , an arbitrary frequency value, the non-trivial optimal level vector is  $I_k^0 = I_k(f_0)$ , and we are interested in figure out the optimal vector for  $f_0 + \delta f$  caused by a small frequency increase  $\delta f$ . The new vector may change its direction to

$I_k^\delta = I_k(f_0 + \delta f)$ . Because of the continuity (Property 3) of  $F_{i|k}(f)$  the closer solution to  $I_k^0$ , from the set  $\beta I_k^\delta$ , must be selected. This procedure must be reciprocal or symmetrical, that is, if  $I_k^\delta$  is known, we must be able to find  $I_k^0$ , for an opposite frequency change  $-\delta f$ . Then, this symmetry guaranties that any equivalent condition along the frequency range can reproduce the same FRF.

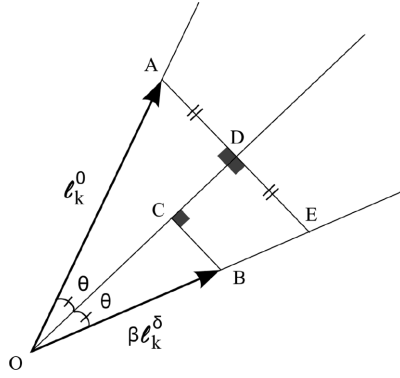
To figure out the closer vector to  $I_k^0$  along the direction  $I_k^\delta$ , it is needed to fix a proper  $\beta$  value. If  $I_k^0$  and  $I_k^\delta$  are parallel, the solution is trivial,  $\beta = |I_k^0|/|I_k^\delta|$ , and consequently, the reference levels are non frequency dependent, forming a constant vector in  $\Lambda$  by the boundary condition  $I_k(f) = I_k(0)$  for all  $f$ . For the non-parallel case, the classic Euclidean distance definition can not be used, because the symmetry condition between the optimal solutions is not satisfied, then we need an alternative distance definition.

Fig. 3 represents the non-parallel case of  $I_k^0$  and  $\beta I_k^\delta$ . We define the distance between these two vectors as the sum of the segments  $AD + CD + BC$ . Here the direction OD is along the bisectrix, and the segments  $AD$ ,  $DE$  and  $BC$  are orthogonal to it. With this definition the minimum distance appears when  $CD = 0$  (Appendix B), therefore the closer solution is found with  $\beta = OE/|I_k^\delta|$ , which means that all solutions must have the same length,  $|I_k^\delta(f)| = |I_k(0)|$ . Thus, all solutions are found on the surface of a  $n$ -dimensional sphere with radius  $|I_k(0)|$  being the symmetry evidently satisfied. This constraint avoids the trivial solution and converts the minimization of the function  $\Delta_k(f)$  in a conditional minimization problem.

The minimization of  $\Delta_k(f)$ , with the constraint  $|I_k(f)| = |I_k(0)|$ , permits to write its corresponding Lagrangian function  $\mathcal{L}$  in the form:

$$\mathcal{L}(L_1, \dots, L_n, \mu) = \sum_{i,j=1}^n (L_i \tau_i - L_j \tau_j)^2 + 4\mu \left( \sum_{i=1}^n L_i - L_0 \right), \quad (9)$$





**Figure 3.** The distance between two level vectors is defined as the sum of the segments  $AD + CD + BC$ . Because the levels are positive, then  $\theta < \pi/4$  and the closer distance become  $AE$ .

where  $L_0 = |\mathbf{I}_k(0)|^2$ ,  $L_i = l_{ik}^2(f)$ ,  $\tau_i = R_{ik}^2(f)$  and  $4\mu$  is a convenient Lagrangian multiplier. The component index  $k$  has been dropped to easy the notation. Then, the equation system  $\partial \mathcal{L} / \partial L_q = 0$ ,  $\partial \mathcal{L} / \partial \mu = 0$ , with  $q = 1, \dots, n$ , is linear for  $L_q$ , its solution exists, the optimum is a minimum, is non-trivial and unique, and it satisfies,

$$\begin{cases} (n-1)L_q \tau_q^2 - \sum_{i \neq q} L_i \tau_i \tau_q + \mu = 0, & q = 1, \dots, n \\ \sum_{i=1}^n L_i = L_0, \end{cases} \quad (10)$$

This system can be written in the matrix form,

$$\mathbb{T}\mathbb{L} = \mathbb{L}_0, \quad (11)$$

being  $\mathbb{T}$  the coefficients matrix of the system,  $\mathbb{L}^T = (L_1, \dots, L_n, \mu)$  and  $\mathbb{L}_0^T = (0, \dots, 0, L_0)$ , giving the solution  $\mathbb{L} = \mathbb{T}^{-1}\mathbb{L}_0$ . See Appendix C for its demonstration and other details. These solutions are frequency dependent and must be solved for each seismic component  $k$ , independently.

The FRF constructed with this approach must be the same for any type of record: displacement, velocity or acceleration (Property 4). It is proved due to in the eqs (1) and (8), by definition, the reference levels have the same physical units than the noise; and because the acceleration spectral amplitudes are  $2\pi f$  times the velocity spectral amplitudes and  $(2\pi f)^2$  times the displacement spectral amplitudes. Hence, the FRF given by eq. (1) remain invariant when records of either acceleration, velocity or displacement are used.

The following steps are used to compute the FRFs.

- (i) The instrument response is corrected for all the records and then filtered in the 0.02–20-Hz range.
- (ii) The earthquake amplitudes are corrected with the factor  $r_i/\bar{r}$ . The spectral amplitude of noise and earthquakes are computed in 0.1 width bins in the 0–20-Hz range. The median of the amplitudes within each bin is selected to represent the bin spectral amplitude. The signal-to-noise ratios  $R_{ik}(f)$  are computed after a weighted filter is used on five-bins moving windows, both in earthquake and noise spectra. The weights are Gaussian density amplitudes for  $-2, -1, 0, 1, 2$  standard deviations, normalized such that the weight sum is one. The first bin is not filtered, and the second one is filtered with the three central Gaussian weights. The last two bins are filtered in similar way than the first two. These first two steps smooth the ratios  $R_{ik}(f)$ .

- (iii) The approximation given by the eq. (8), for each component  $k$ , is used to compute  $L_0 = |\mathbf{I}_k(0)|^2 = \frac{1}{4} \sum_i N_{ik}^2(\epsilon)$ , with  $\epsilon = 0.05$  Hz, which is the central frequency of the first bin.
- (iv) The optimal levels for each bin-central frequency are computed as the solutions of the equation system (10).
- (v) After knowing the levels for the whole frequency range, the FRFs at each station are computed using the eq. (1). These FRFs are computed for each earthquake. Finally, the FRF of each station and component are computed as the median of the FRFs computed with individual earthquakes.

The paroxysms cause seismic waves, infrasound waves and pyroclastic flows. All of them are simultaneously recorded at each station. A number of corrections must be made before trying to locate the seismic paroxysmal sources. If cultural activity and pyroclastic flows are included in the records, which produce high frequencies surface waves, the site effect correction can amplify them. These signals occur mainly above 8 Hz and so this frequency range is filtered out in our analysis. Airwaves coupled in the ground, produced by paroxysmal jets, are also present in the seismic records. In the next section, before locating the eruptive tremors, we compute the coherence between the observed infrasound and seismic waves in order to identify the frequencies where such coupling occurs.

### 2.3 Airwave coupling

Airwaves are generated by paroxysmal jets, which are a mixture of pyroclasts and gases ejected into the atmosphere (Matoza & Fee 2018). Such airwaves impact the ground and part of their energy is transmitted to it. If this coupling process is strong enough, it may dominate the recorded seismic signals (Palacios *et al.* 2016). We investigate whether such coupling exists using the squared coherence  $K(f)$  between the infrasound ( $x(t)$ ) and each seismic component ( $y(t)$ ), which is defined by the Fourier transform of their cross-correlation,  $G_{xy}(f)$ , and the Fourier transform of their autocorrelations,  $G_{xx}(f)$  and  $G_{yy}(f)$ , namely (Buttkus 2000):

$$K(f) = \frac{|G_{xy}(f)|^2}{|G_{xx}(f)||G_{yy}(f)|}, \quad (12)$$

being values between zero and one. To have a map of its temporal evolution in each paroxysm, a coherogram of  $K(f)$  is computed with 60-s moving windows, overlapped 50 percent.

### 2.4 Seismic source locations

Volcanic edifices are highly complex and heterogenous geological structures, which effect the seismic ray paths, modifying amplitudes, path lengths and travel times. To take into account such effects, the 3D  $P$ -wave tomography of Tungurahua computed by Molina *et al.* (2005) is used to estimate both the source-station path lengths and their travel times.

The tomographic model is a 3D array of velocity information with 500-m node spacing in the three dimensions, within a domain with horizontal dimensions between  $-10$  and  $+10$  km centred around the location  $78.44^\circ\text{W}$ ,  $1.47^\circ\text{S}$ , WGS84, close to the summit. We interpolate these velocities between nodes with the Ordinary Kriging (OK) method (Appendix D), which takes into account the spatial cross-correlation of the information, yielding a denser 3D grid with 100-m node spacing (forming an array of  $\sim 5.6 \times 10^6$  nodes). A vertical and cylindrical domain of 10 km radius with and a maximum depth of 15 km below the sea level, and height up to the topographic surface is used in the seismic locations.

To compute the velocity at an arbitrary point, a subset of its neighbours within the denser 100-m node spacing tomography is selected, and the inverse-distance interpolation method is applied. Then, using Fermat's principle (Kot 2014), for each node of the 500-m node spacing tomography, the travel time and ray path length to each seismic station are computed and then interpolated to 100-m node spacing by the OK method. This last step produces one dense 3D array for path lengths and another for travel times, for each station, both with 100-m node spacing. Appendix D explains further interpolation details.

Far-field approximations (Madariaga 2015) are commonly applied in seismic source location methods (Battaglia 2003; Kumagai *et al.* 2010; Morioka *et al.* 2017; Walsh *et al.* 2017). Similarly, assuming isotropic point sources, we denote with  $\xi_{ik}$  the far-field approximation, from a station  $i$ , of the energy rate emitted by a source at its location  $k$ . This rate is proportional to the wave velocity  $c$  in any spatial point (Boatwrite 1980; Stein & Wyssession 2003). If  $r_{ik}$  is the length of the curved ray path between the source and the station, here considered as the distance between them, the geometrical spreading—or elastic attenuation—of the energy is proportional to the inverse of this squared distance (Chapman 2004). Then, estimating the average wave velocity as  $c = r_{ik}/\tau_{ik}$ , being  $\tau_{ik}$  the travel time along the ray path, taking into account the elastic and inelastic attenuations, and the contribution of P and S waves,  $\xi_{ik} = \xi_{ik}^P + \xi_{ik}^S$ , the far-field approximation can be written as

$$\xi_{ik} = 4\pi\rho r_{ik}^3 \tau_{ik}^{-1} \left\{ \int (A_z)_i^2(f) \exp[2\pi f \tau_{ik} Q^{-1}] df + \frac{1}{\sqrt{3}} \int (A_h)_i^2(f) \exp[2\pi f (\sqrt{3}\tau_{ik})(4Q/9)^{-1}] df \right\}, \quad (13)$$

where the volcanic edifice is considered as a Poisson's solid, and consequently we have the velocity ratio  $v_P/v_S = \sqrt{3}$  (Stein & Wyssession 2003) and the quality factor ratio  $Q_P/Q_S = 9/4$  (Butler 2020). Here,  $\tau_{ik}$  is the travel time of P waves,  $Q = Q_P$ ,  $A_z^2$  the vertical power spectrum of particle velocity records,  $A_h^2$  the sum of both horizontal power spectra, and  $\rho$  is the edifice-average density. The limits for the integral depend on the paroxysm and are selected as frequency ranges where no ground-coupling effects are observed. In practice, the integral is replaced by a sum of power spectrum amplitudes, accumulated at intervals of  $df \sim \delta f = 0.1$  Hz width, satisfying the Parseval's theorem (Buttkus 2000).

The energy from a selected source arrives at a different time to the stations, depending on the ray path to each one. The traces used in the location should be cut in windows depending on such time differences, before computing  $\xi_{ik}$ . But, implementing a cut process with these differences is computationally expensive, because of the large number of nodes that our arrays form. Due to the quantile, 0.99 of the arrival time differences computed from the denser travel time array is 2.1 s for the Tungurahua seismic network, we cut 60-s windows, with common initial time and apply a cosine taper of 5 s at both window borders, in order to reduce the errors introduced by the arrival time differences. It left at least  $\sim 48$  s of common source information per window.

Because the energy rate emitted at the source,  $\xi_{ik}$ , is actually independent of the station  $i$  used, any difference between a pair of stations should in theory be zero, and in practice, approximated by a minimum value, if the right source location is selected. This criterion is represented by the following residual definition to be computed for each source-node  $k$ ,

$$D_k = \frac{1}{(4\pi\rho \delta f)^2} \sum_{i>j} (\xi_{ik} - \xi_{jk})^2, \quad (14)$$

where the constant  $(4\pi\rho \delta f)^2$  is canceled out in the residual computation. Thus, the residual unit is  $(\text{m}^5 \text{s}^{-3} \text{Hz}^{-2})^2$ . Note here that any constant factor, which is not dependent on some source property or relation with the stations, defines only a common residual scale for all the nodes. Therefore, two or more source-nodes can be compared and that with the minimum residual can be selected.

It is well known that the quality factor  $Q$  has a strong influence in the seismic locations (Kumagai *et al.* 2010). To select the best  $Q$  of each paroxysm, we compute the locations with  $Q$  values between 5 and 60, one-unit apart between 5 and 20, five-units apart between 20 and 50, and with  $Q = 60$ . Then, we apply two selection criteria. First, it is expected that the best  $Q$  is related to smaller residuals, and second, that the locations form tighter clusters, because all the tremor windows share a very similar physical process. Hence, the best  $Q$  is selected as the value that satisfies both criteria, simultaneously.

Given a paroxysm, to explore both how much tighten its cluster of locations is, and the behaviour of its location residuals as function of  $Q$ , optimal locations with minimum residual less than their quantile 0.95 are selected, in order to prevent any outlier effect. The spread value  $s = s(Q)$ , defined as the average of distances between the source locations and their geometrical centroid, is computed, and the following normalized and positive index is also computed:

$$\beta_s(Q) = \frac{s - \min(s)}{\max(s) - \min(s)}. \quad (15)$$

The base-10 logarithm of the minimum-residual average  $m = m(Q)$ , and the index

$$\beta_m(Q) = \frac{m - \min(m)}{\max(m) - \min(m)}, \quad (16)$$

are used to represent the behaviour of residuals as function of  $Q$ .

## 3 RESULTS

### 3.1 Site effect corrections

#### 3.1.1 Evidence of site effect in paroxysmal records

Site effects are caused by shallow structures close to a given station. We have assumed that the seismic noise wave field stores information about the site, independently if it is caused by backscatterings, in local heterogeneities, or by topography or other geological conditions. If this is true, any wave field crossing local structures may be modified in similar way than the seismic noise. This actually occurs and can be detectable in volcanic events, regional earthquakes, or paroxysmal tremors. Because of the gravity, the geological structures are horizontally more spread than vertically, usually forming horizontal layers in a 3D space, then, one of the best ways to show this effect is computing the spectral ratio of horizontal to vertical components ( $H/V$ ). As an example, Fig. 4 presents the spectral ratio of seismic noise (black) and the eruptive tremor of the paroxysm E1 (red). The shapes of noise ratio curves are station dependent, as may be expected; however, they are roughly reproduced by the paroxysmal tremor. This similarity is evidence of a common origin, the local geological structure. If the similarity is measured with the Pearson correlation coefficient, given at the right top of each panel, it decreases to 0.0282 (BCUS), 0.1503 (BMAS1) and  $-0.0386$  (BRUN) after site effect correction, as would be expected. Evidently, other factors like path and source effects, or ground-coupled airwaves, must be considered to get tremor locations, and should explain other differences of these ratios. Thus, next subsections show details of FRF computation and their effects on seismic records.

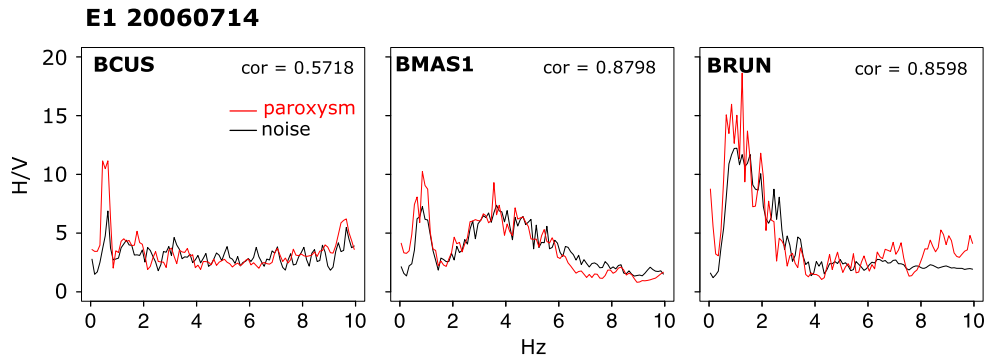


**Figure 4.** Horizontal to vertical amplitude spectral ratio of seismic noise (black) and eruptive tremor (red) of the paroxysm E1, for each seismic station. The corresponding Pearson correlation coefficient is given at the right top of each panel.

### 3.1.2 Frequency response functions

Fig. 5 presents the FRFs of vertical (Z), North (N) and East (E) components computed with the eq. (1), which transforms the noise spectrum with frequency dependent denominators. The FRFs obtained with the 41 earthquakes are represented by grey lines, and their median by red lines. As it is expected, higher frequencies are mainly attenuated at all the components (Property 1). It is also observed that the amplification factors are smaller in vertical components compared with the horizontals. In addition, horizontal components are mainly amplified in the 1–5-Hz range in all the stations, being the largest in BRUN.

Up to this point, the FRFs have been computed using the whole record of each earthquake, which includes *P*, *S* and coda waves. Their windows start roughly 5 s before the *P*-wave arrival and end at the time described in Table A1. Because we assume that these records are dominated by body waves, we explore the effect of computing the FRF either only with *P* waves, or with *P* and *S* waves before the arrival of surface waves, or with *S* waves and the remaining coda of the records. Because surface waves are slower than *S* waves, and because their propagation roughly starts at the epicentre, their arrival time must be larger than  $t_g = \left(h + \sqrt{H^2 - h^2}\right) t_s / H$ , where  $h$ ,  $H$  and  $t_s$  are the magnitude of the source depth, the hypocentral distance and the arrival time of *S* waves, respectively. This threshold would be the arrival time of surface waves if they would be as faster as *S* body waves. As result, the obtained  $t_g$  values are mainly between 5 and 10 s after the arrival of *S* waves.

Fig. 6 compares the FRFs from different windows of earthquakes. The plot is in logarithm scale to highlight the differences at low frequencies and to explore the effect of surface waves. Each grey line is the FRF computed with the whole earthquake record and all them provide the FRFs range of variation, which can be taken as a measure of uncertainty. The final FRF (blue line) is obtained as the median of the grey lines. As it is possible to observe, even at low frequencies, different earthquake windows used in the FRFs computation do not cause strong differences. At least all them are within the expected range of variation, or uncertainty. Even more, very low differences between FRFs are observed within the 0.4–2.5-Hz frequency range, which plays a key role in the tremor source location, as is described in the next section. This result supports our hypothesis that the surface waves, for the group of selected regional earthquakes, contribute with less energy than body waves. Therefore, in next sections, the FRFs computed with the whole earthquake records are only used.

Finally, the comparison of the FRFs, between components, at each station, and between stations are shown in the Fig. 7. It is

possible to observe that horizontal FRFs are always larger than the vertical FRFs. Left-hand panels present the stations with larger horizontal amplifications. With BPAT as exception, both horizontal components amplify in similar way. The difference in the resonance frequencies (frequency for the maximum FRF value) of the horizontal component in BPAT suggests the existence of a geological structure that need to be explored in future studies.

### 3.1.3 Records corrected for site effects

As an example of a typical result, the seismic traces of the EQ06 earthquake (2011.07.22 08:20:38, 4.2 ML<sub>v</sub>) before and after site effect corrections are presented in Fig. 8, where each panel is plotted at a fixed scale for comparisons. Clearly, the corrections produce less differences between stations for each corresponding component. Even more, at each station, the usual strong difference between vertical and horizontal components decreases significantly after the site correction, in agreement with the Property 5. Such similarities appear despite the fact that the seismic components have been independently corrected.

To evaluate the improvement of any site correction method, Palacios *et al.* (2015) use the relative change of residuals (section 3.5 therein). This quantity, called relative improvement, has a maximum value 1 and may be considered as a similarity measure. Larger positive values represent better similarities, for zero no change appear, and negative values represent a worsening, or an increase of differences. Fig. 9 represents the similarities of our 41 earthquakes. The first five earthquakes were used to compute the FRFs of BCUS and BMAS1. The worst cases occur with the vertical component of EQ03 and EQ09, and additionally, it is observed that vertical components are harder to improve compared with the horizontal ones. Table 4 in Palacios *et al.* (2015) shows the most of the similarity values in the range between 0.1 and 0.3, whereas the generalization here proposed uses frequency-dependent reference levels and produces better results with values between 0.3 and 0.5, mainly. At the end, this result means that here we have better FRFs to represent the site responses.

The influence of site corrections on the paroxysmal tremors is significant. Fig. 10 shows the case of BRUN station, which is the only station that recorded all the eruptions. The results for the other stations are similar. Before the site corrections, the paroxysmal energy appears concentrated below 5 Hz (black curves). However, after the site corrections, the energy is concentrated below 2 Hz (red curves). It means that one influence of the sites is the spectral spreading of the source energy, mainly caused by the amplification of the horizontal components at frequencies below 5 Hz, as is shown in Fig. 5.

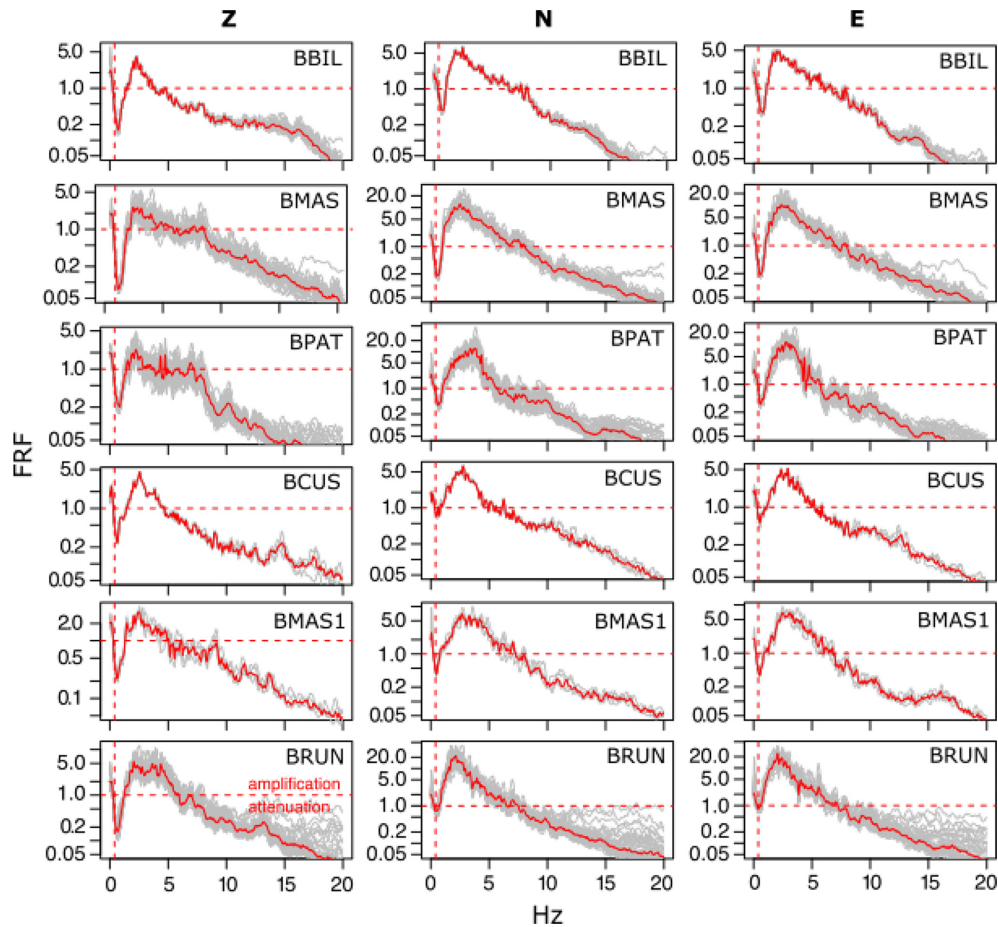


**Figure 5.** Amplitudes of site FRFs, depending on the station and component. Each grey curve is a FRF computed using a distant earthquake. The red curves are the corresponding medians. At horizontal red dashed lines the FRFs reach the value 1, larger values represent amplifications and smaller attenuations. The vertical dashed lines are at 0.4-Hz limit.

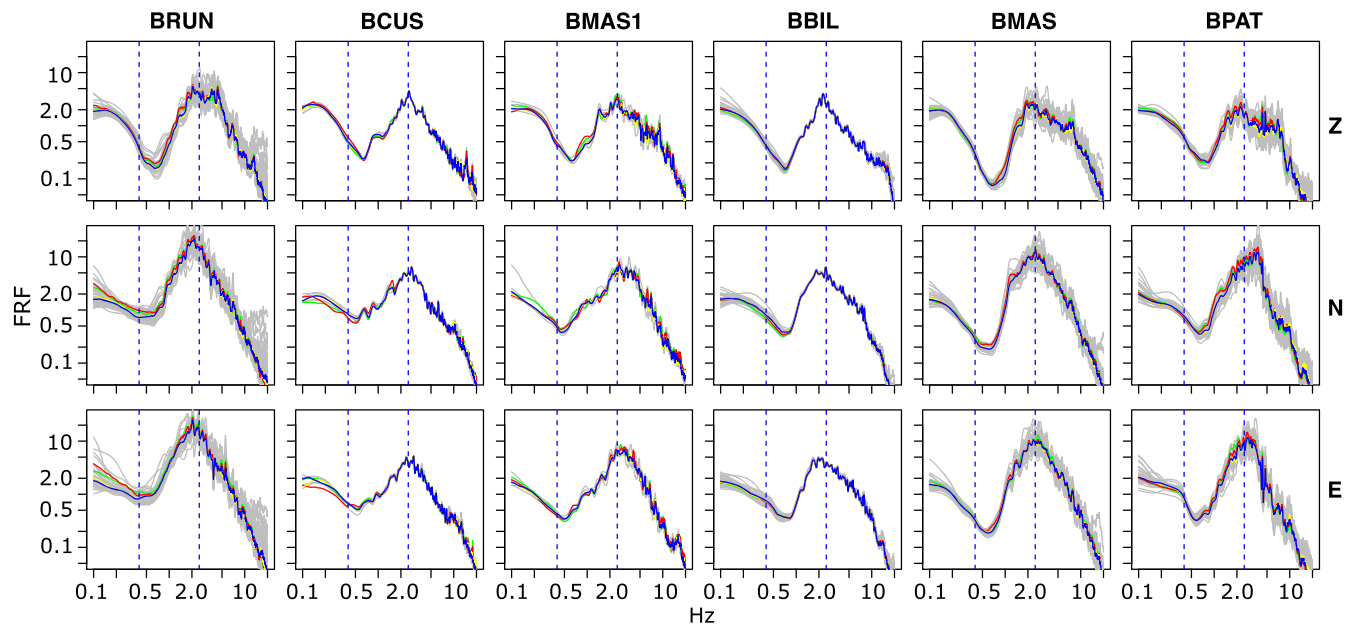


**Figure 6.** FRFs computed with different earthquake windows. Each grey FRF is obtained from the whole earthquake record. Blue FRFs are obtained with whole earthquake records (median of grey FRFs). Green FRFs are medians obtained only with P wave records. Red FRFs are medians from record windows including P waves and S waves, but before the surface wave arrivals. Yellow FRF medians arise from S waves and the remaining coda. The vertical blue dashed lines limit the 0.4–2.5 Hz frequency range.



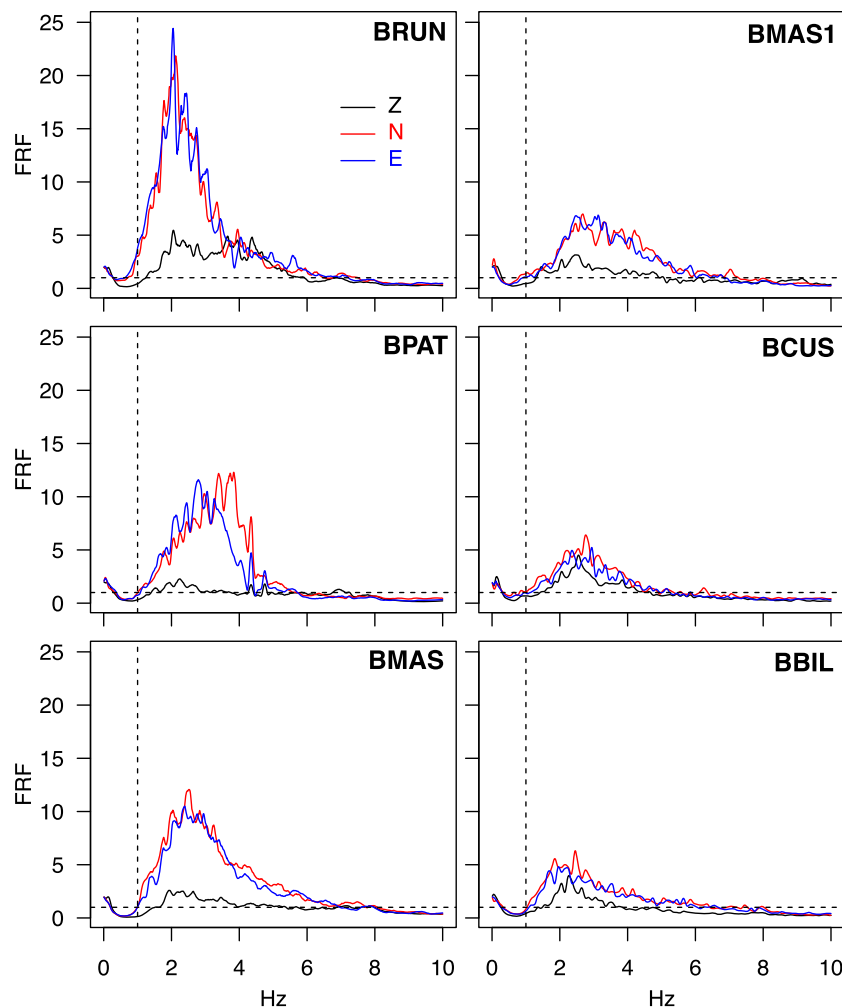


**Figure 7.** Comparison between Vertical (black), North (red) and East (blue) FRFs for each station. The horizontal dashed line are at the level 1, to separate site amplifications from attenuations. The vertical dashed lines are at 1 Hz.

The site correction tends to eliminate such spreading, showing that the paroxysmal sources are actually less polychromatic.

### 3.2 Airwave coupling

The highest coherences are observed at BRUN station, mainly between infrasound (BDF) and vertical components (BHZ). Fig. 11 presents the results for the 10 paroxysms E1–E10. The coupling, represented by high coherence values, appears in bands of the frequency domain. We consider null or weak coupling when the squared coherence values are  $\leq 0.4$ . Note that a  $\sim 0.2$  squared coherence value is produced by pure random time series. Fig. 11 also shows that the band  $\sim 0.4$ – $2.5$  Hz does not include significant couplings, which is coincident with the spectral interval where most of the seismic energy of the paroxysms is concentrated (Fig. 10), suggesting that such energies are dominated by body waves from the seismic sources of the tremors.

The frequency bands of the paroxysms where weak or no couplings occur are presented in Table 2. These intervals, for a particular component, are computed as the intersection of the no coupling intervals of all the stations. Then, for each paroxysm the common band to all the components is also determined by intersection and presented in the last column of the table. Because this result is

identical to the BHZ column (with E5 as an exception) it is evident that the ground-coupling effects are better described by vertical components, as might be expected.

The differences in the no coupling frequency bands between paroxysms may be related to several factors like wind conditions, depth of the fragmentation region, changes in the vent morphology, between others. To analyse such factors is out of the scope of this paper.

### 3.3 Seismic source locations

As convention, the location results presented in this paper use signed depths, relative to the sea level, being upward positive and downward negative.

#### 3.3.1 The influence of $Q$

$Q$  has a significant influence in the location results. Fig. 12 shows the locations of the paroxysm E8 for the values  $Q = 6, 12, 25$  and  $50$ , in panels (a)–(d), respectively. The locations form tighten clusters for low  $Q$  values, being vertically better aligned with the volcanic vent for  $Q = 12$ . When the  $Q$  value increases, the group of locations migrates to shallow depths beneath the NW flank.

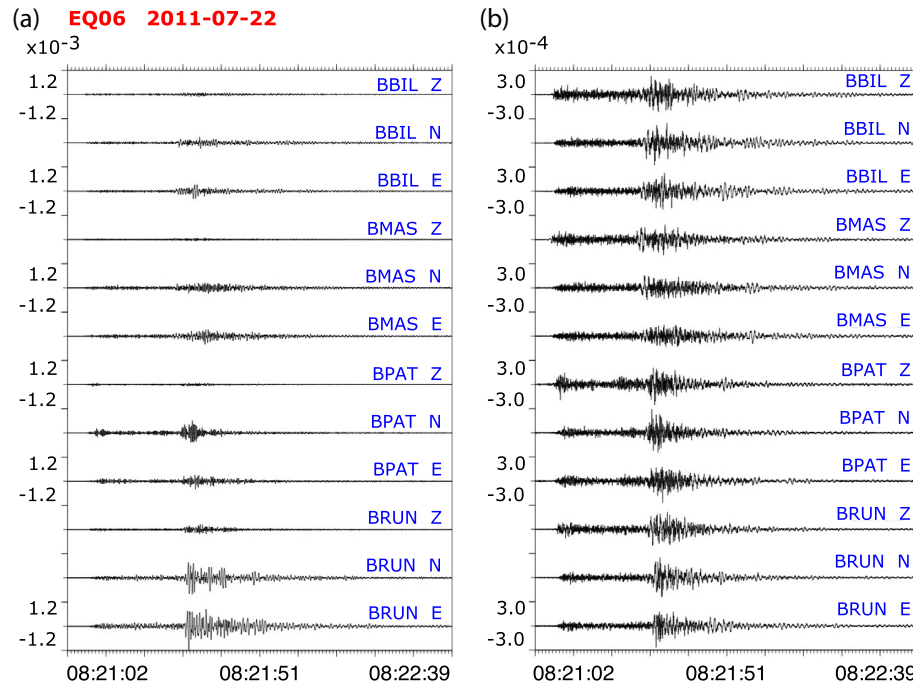


**Figure 8.** Seismic component of velocity amplitudes ( $\text{m s}^{-1}$ ) of the EQ06 earthquake. Panel (a) records of seismic traces at all the stations. Panel (b) seismic traces after site effect corrections.

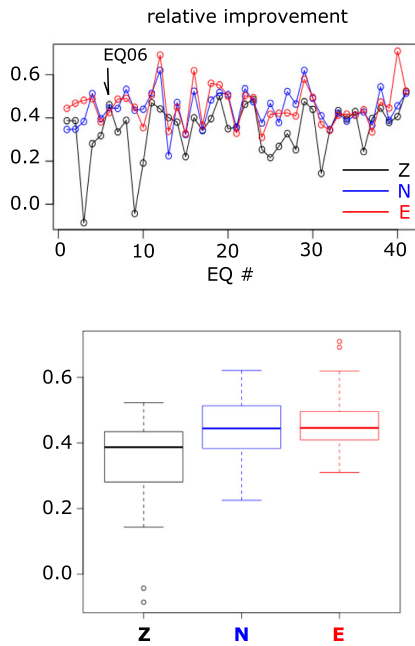


**Figure 9.** Relative improvement of 41 earthquakes after site corrections. In the top panel, the values for each earthquake and component are represented. The bottom panel shows the box and whisker plots of relative improvements. EQ06 earthquake, plotted in Fig. 8, is a case with improvements close to the averages.

The information of each panel includes the value ‘min.res mean’ which is the average of all minimum residuals of the locations. It is observed that this value decreases while  $Q$  increases. On the other hand, the ‘spread’ value increases when  $Q$  also increases. These behaviours are observed in all the paroxysms here studied (Fig. 13). Such a result is actually unexpected, because we may think that

better locations are related to both lower residuals and low spreads, assuming that the seismicity comes from sources spatially related and closer between them. Consequently, an uncertainty effect arises, which basically says that while more precise the locations are (low residuals), less precise the group identification of sources is (high spreads).

If it is considered that a tighten cluster of locations and low residuals are properties of good locations, it is possible to find an intermediate  $Q$  value that satisfies both criteria, which is related to the  $Q$  of the intersection point of both indices,  $\beta_m(Q)$  and  $\beta_s(Q)$ , because there both criteria are satisfied simultaneously. The intersection is found where the function  $\beta(Q) = |\beta_m(Q) - \beta_s(Q)|$  gets its minimum value. As a result, the best  $Q$  values are between 9 and 16 (Fig. 13).

### 3.3.2 The paroxysm locations

The absolute residual model, eq. (14), and the best  $Q$  values found in the previous section are used here to plot the locations of the seismic tremor for each of the 10 paroxysms. Given 60-s window of tremor, the residual value is computed for each 100 m apart node within the volcanic edifice, and the node with the minimum value is selected as the source location. The paroxysmal locations appear in Figs 14 and 15. The information at the lower left part of each panel shows the number of locations, the average of their minimum residuals and the spread value. Table 3 is the summary of the paroxysm parameters. For each paroxysm, the locations with residuals less than the quantile 0.95 of minimum residuals were selected. The depth range, formed by the quantile 1 percent and the maximum value, is between  $-5.4$  and  $+4.5$  km respect to the sea level. The more shallow locations arrive a few hundreds metres to the north of the vent. Only a single location (that is associated with E3) appears much deeper with a depth of  $-7.1$  km, distant from the group of locations. Although the paroxysm locations roughly

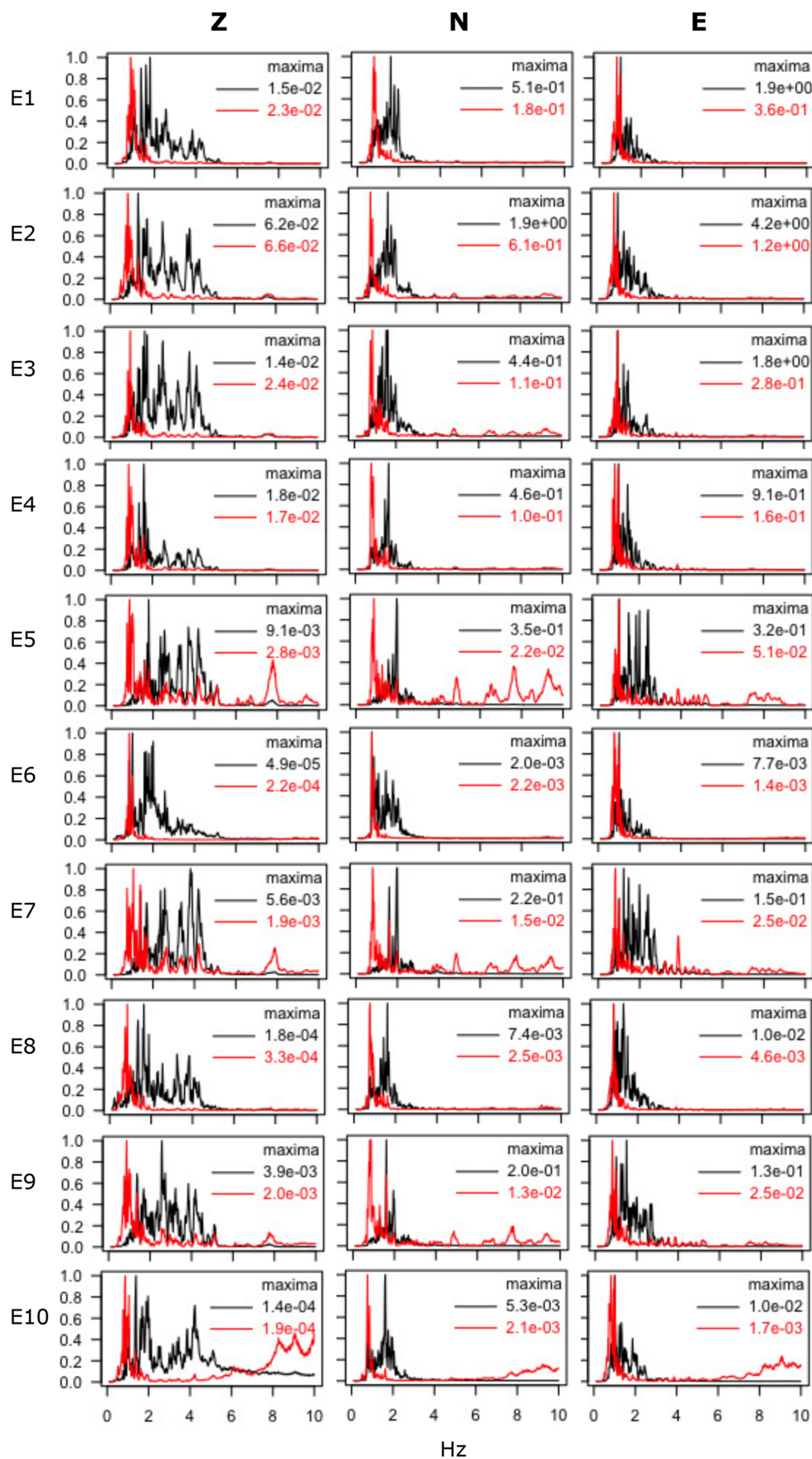


**Figure 10.** Power spectra of each component and paroxysm, before (black) and after (red) site corrections for BRUN station. The maximum spectral amplitudes ( $\text{m}^2\text{s}^{-2}\text{Hz}^{-1}$ ) appear at the top-right corner of each panel.



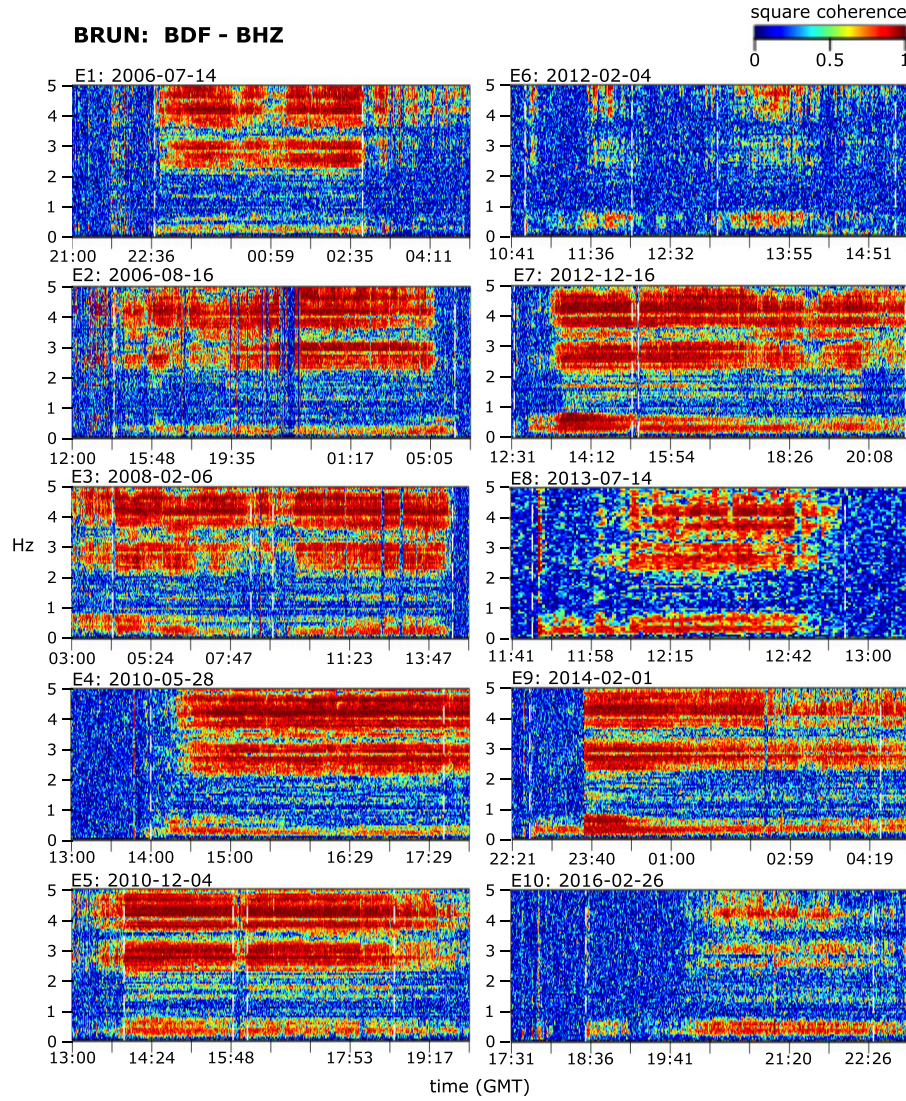


**Figure 11.** Coherograms, between BDF and BHZ components at BRUN station, of the paroxysms E1–E10, computed for 60-s moving windows, using two 5-length modified-Daniell kernels, with 10 per cent taper. The squared coherence values are represented in colour scale.

**Table 2.** Frequency bands (Hz) without airwaves ground-couplings.

Paroxysm	BHZ	BHN	BHE	All the components
E1	0.4–2.0	0.2–3.5	0.4–2.5	0.4–2.0
E2	0.4–2.2	0.2–3.5	0.4–2.5	0.4–2.2
E3	0.9–2.0	0.4–2.5	0.4–2.4	0.9–2.0
E4	0.4–2.0	0.1–2.0	0.4–2.3	0.4–2.0
E5	0.7–1.8	0.1–1.6	0.4–1.4	0.7–1.4
E6	1.0–2.5	0.1–4.5	0.1–4.2	1.0–2.5
E7	0.8–2.0	0.7–2.0	0.5–2.1	0.8–2.0
E8	0.9–2.1	0.1–2.1	0.6–2.1	0.9–2.1
E9	1.1–2.1	1.0–2.5	0.6–2.5	1.1–2.1
E10	0.8–2.2	0.1–3.5	0.5–3.0	0.8–2.2

cover the same region within the volcanic edifice, some differences appear between them.

All the paroxysms, with E4 as the exception, are concentrated at depths between  $-1$  and  $+2$  km (Table 3, fourth column). Actually, we can identify three types of distributions for the number of locations as function of depth (Fig. 16). The first group are those forming unimodal distributions (E1–E3, E5, E6 and E10) with their

peaks within the  $[-1, 2]$  km depth range. The second group (E7–E9) has bimodal distributions, with the main peak within the  $[-1, 2]$  km depth and the second peak within the  $[-5, -3]$  km depth range (Table 3, third column). And the third group includes only the paroxysm E4, which has the major part (63.1 percent) of its locations below the  $-1$  km depth. This classification is also consistent with the centroid depth (Table 3, seventh column): the first group has centroids above the sea level, the second has below the sea level, and E4 has a deeper centroid. In addition, E7, E8 and E9 present a clear sub-cluster around the  $+1.0$  km depth.

To plot the location of a single window together with its residuals we follow the next steps. Because we deal with very small residual values, the base-10 logarithm of them is computed, then the values are displaced by their minimum to zero, and the result is divided by their 0.95 quantile. Finally, any value larger than 1 is set as 1. Thus, the colour map, like the bottom panel in Fig. 21, uses the colour range between zero and one, relating them to the minimum residual and the 0.95 quantile, respectively. An option to produce a set of plots to compare  $M$  locations, is to compute the base-10 logarithm of the residuals; then, their corresponding minima  $\{m_1, \dots, m_M\}$  and their 0.95 quantiles  $\{q_1, \dots, q_M\}$ . The common value



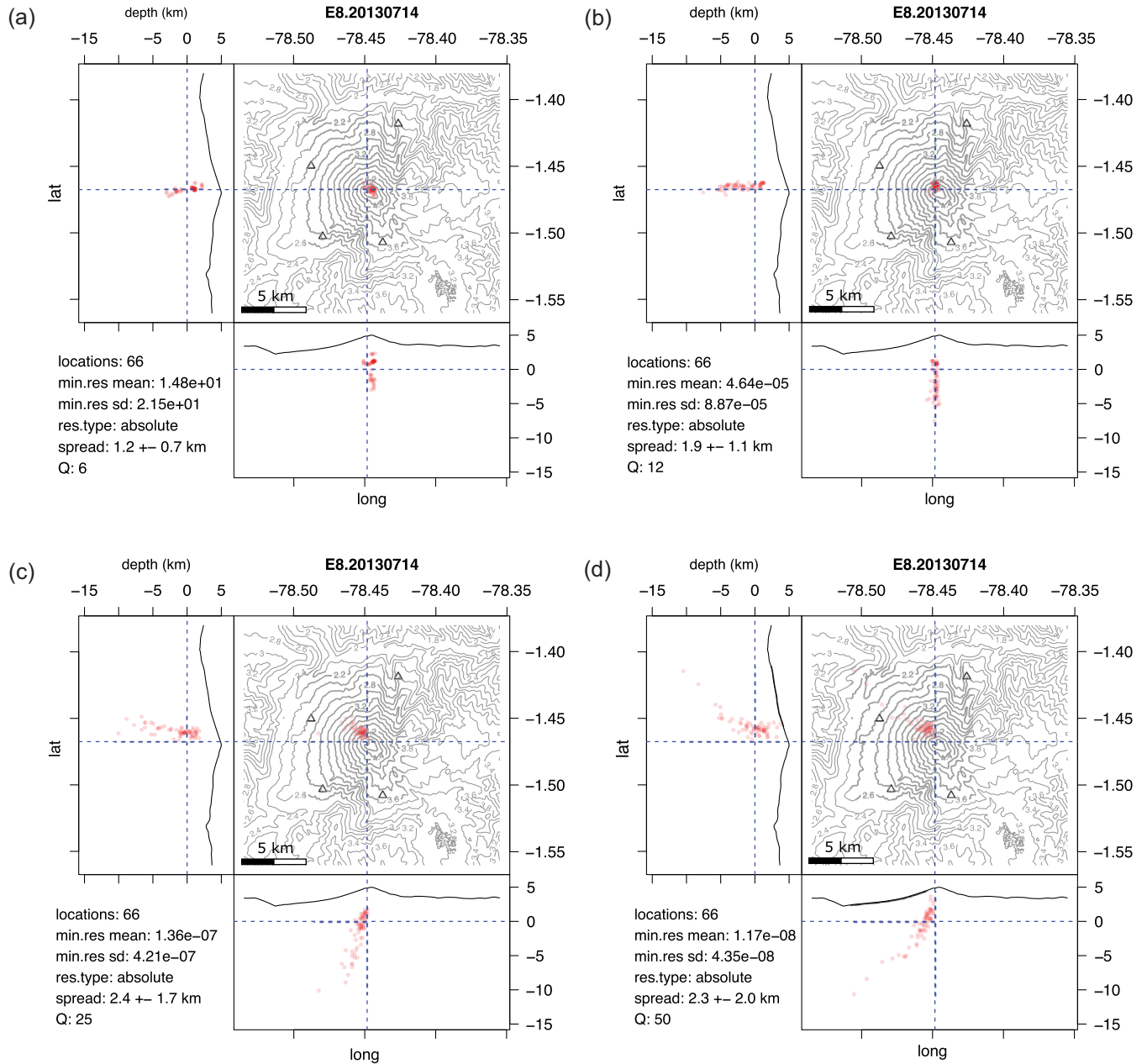


**Figure 12.** Changes in the locations of the paroxysm E8 when  $Q$  gets the values 6, 12, 25 and 50. Blue dashed lines cross the volcanic vent and the sea level. The triangles represent station locations.

$D = \min\{m_1, \dots, m_M\}$  is used to displace the logarithm-residuals of each location, and the common value  $S = \max\{q_1, \dots, q_M\} - D$  is used as denominator to scale them. Finally, any value larger than 1 is set as 1, which allows to fix a common plotting colour scale between 0 and 1. Fig. 17 shows the comparison of two locations of the paroxysm E5, a case where the shallow location has the smaller residual.

## 4 DISCUSSION AND CONCLUSIONS

### 4.1 Site effect corrections

Site effects, as the seismic response of some location, comprises several wave phenomena: amplifications or attenuations due to

constructive or destructive interference, ray path bending caused by refractions (Yoshida 2015), scatterings and back-scatterings by geological structures (Aki 1969; Sato et al. 2012). To understand these phenomena, several models have been proposed. Safak (1995) develops an horizontal layer model, which predicts main and secondary resonance frequencies. But this model can not successfully explain real data, mainly because it does not take into account reflections at regional borders, which is very common phenomenon in alluvial and sedimentary basins (Cruz-Atienza et al. 2016). These border reflections can also generate stationary waves within the basins (Semblat et al. 2005), as experiments and models on plate composites predict (Farsani et al. 2020). On the other hand, models based on random scatter distributions (Sato et al. 2012) use the coda waves of earthquakes and a reference location, being it located at some outcrop surface, to define the FRFs (Mayeda et al. 1991; Kato

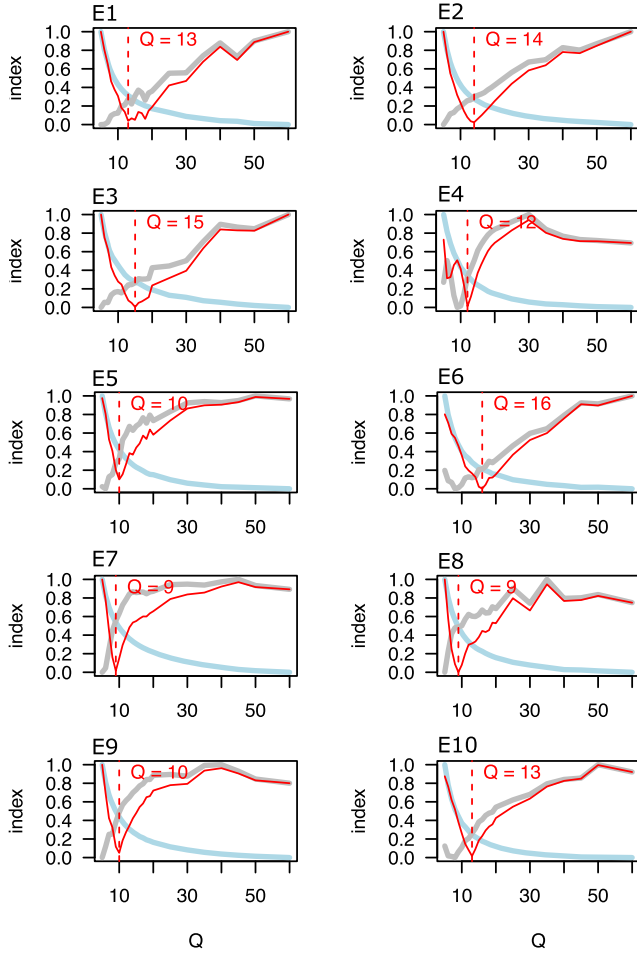


**Figure 13.** Indices of the minimum residual  $\beta_m(Q)$  (blue line) and spread  $\beta_s(Q)$  (grey line) as function of  $Q$ , and best  $Q$  value selection for each paroxysm. The continuous red line is the function  $\beta(Q) = |\beta_m(Q) - \beta_s(Q)|$ , with  $Q \in [5, 60]$ .

et al. 1995). Consequently, this approach is limited by the nature of the reference location, and the FRFs might change if a different reference location is selected.

Hence, to take into account the full variety of wave phenomena, Palacios *et al.* (2015) assume that the seismic signals actually store all information caused by those phenomena, and normalize the seismic noise based on the site excitation caused by distant earthquakes, to define the FRFs. This process produced constant, frequency-independent, reference levels. In this paper, we improve on this noise normalization by allowing the reference levels to depend on frequency, which produces better results. The main reason for this improvement is because the site effects, which is common information in noise and earthquakes records, is cancel out during the computation (eq. 2), independently of their physical causes, and without the necessity of a reference location. Thus, the computation method of the FRFs here proposed improves our interpretation of the site corrected records, like those from the paroxysms here studied (Fig. 10).

The eqs (8) and (10) suggest that the results that define the FRFs depend on the seismic networks selected, and consequently two different sets of FRFs might not be comparable. To provide an evaluation of such dependence, first, it is needed to observe that better-defined FRFs are obtained while more stations (comparison pairs) and earthquakes (site excitations) are used, which implies that

a minimum of three stations is needed. In this study two different seismic networks are available, a first with three stations (BRUN, BCUS, BMAS1) excited by five earthquakes, and a second with four stations (BRUN, BBIL, BMAS, BPAT) excited by 36 earthquakes. Due to BRUN is the common station to both networks, its FRFs can be compared. Fig. 18 shows the results. The grey lines represent the FRFs calculated from each earthquake. The black FRFs are only computed with the first network (and five earthquakes), the red FRFs are only computed with the second network (and 36 earthquakes), and the blue FRFs are computed with both networks (the same as those in Fig. 5). Roughly below 2 Hz and above 5 Hz all the FRFs are very coincident. Some differences appear between 2 and 4 Hz but within the range of variation (grey lines). The major difference appears for only the vertical component close to 4 Hz. If we assume that this difference is caused by low information provided by the first network, the result suggests that more stations and earthquakes are convenient to get comparable FRFs.

For the paroxysm locations, Fig. 19 shows the consequence of using records corrected and not corrected for site effects, in both cases computing with the best  $Q$  values (Table 3) and the absolute residual model (eq. 14). The blue dots represent locations not corrected for site effects and are located  $\sim 1$  km at the North of the red locations, which have been corrected for site effects. This epicentral difference is expected because the station BRUN amplifies the seismic waves more than the other stations (Figs 5 and 8—panel a). Because the location method is based on amplitudes, the sources appear closer to the stations with larger amplitudes, causing, in this case, northward displacements. Similar effects are observed for the other paroxysms. In addition, because for each paroxysm the average of the minimum residuals of blue locations is much larger than that of red locations (Table 4), we conclude that using records corrected for site effects provide much better locations.

## 4.2 Airwave coupling

Ground-coupled airwaves (Ben-Menahem & Singh 2000; Allard & Atalla 2009) caused by volcanic eruptions (Matoza & Fee 2018; Battaglia *et al.* 2019) can be detected using, for instance, cross-correlation functions, in time domain, between infrasound and seismic records, from sensors at the same location (Ichihara *et al.* 2021). But the cross-correlation can change depending on the wave frequency content, then, the normalized Fourier transform of such cross-correlation, which is the coherence (Sciotto *et al.* 2011; Canata *et al.* 2013; Matoza & Fee 2014; Palacios *et al.* 2016; McKee *et al.* 2018), is more suitable to identify frequency ranges of airwave couplings. In our case, we identify these ranges to limit our analysis where the coherence is null or weak, being they roughly coincident with the ranges where the paroxysmal tremors concentrate the major part of their seismic energy, after site effect corrections.

## 4.3 Seismic source location

### 4.3.1 Equivalent residual expressions

The absolute residual (eq. 14) for the source-node  $k$ , without its constant factor  $(4\pi\rho\delta f)^{-2}$ , written here as  $\Delta_k$  (do not confuse with the residual of the section 2.2), for a seismic network of  $n$  stations, has the equivalent expressions:

$$\Delta_k(r_{1k}, \dots, r_{nk}) = \frac{1}{2} \sum_{i,j=1}^n (\xi_{ik} - \xi_{jk})^2 = n \sum_{i=1}^n (\xi_{ik} - \bar{\xi}_k)^2, \quad (17)$$

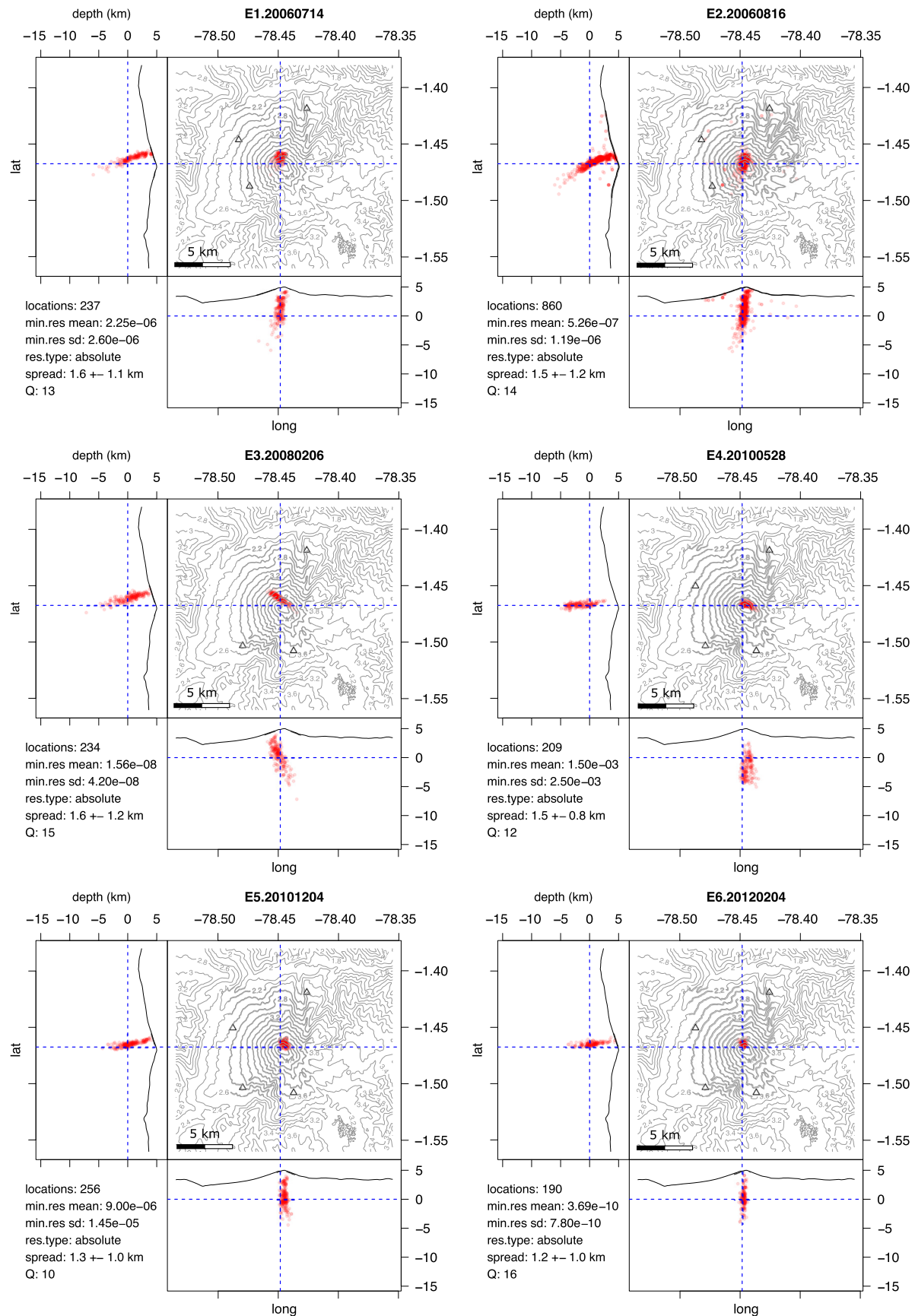


**Figure 14.** Locations of seismic sources of the paroxysms E1–E6. Blue dashed lines cross the volcanic vent and the sea level. The triangles represent the seismic stations used for the locations.

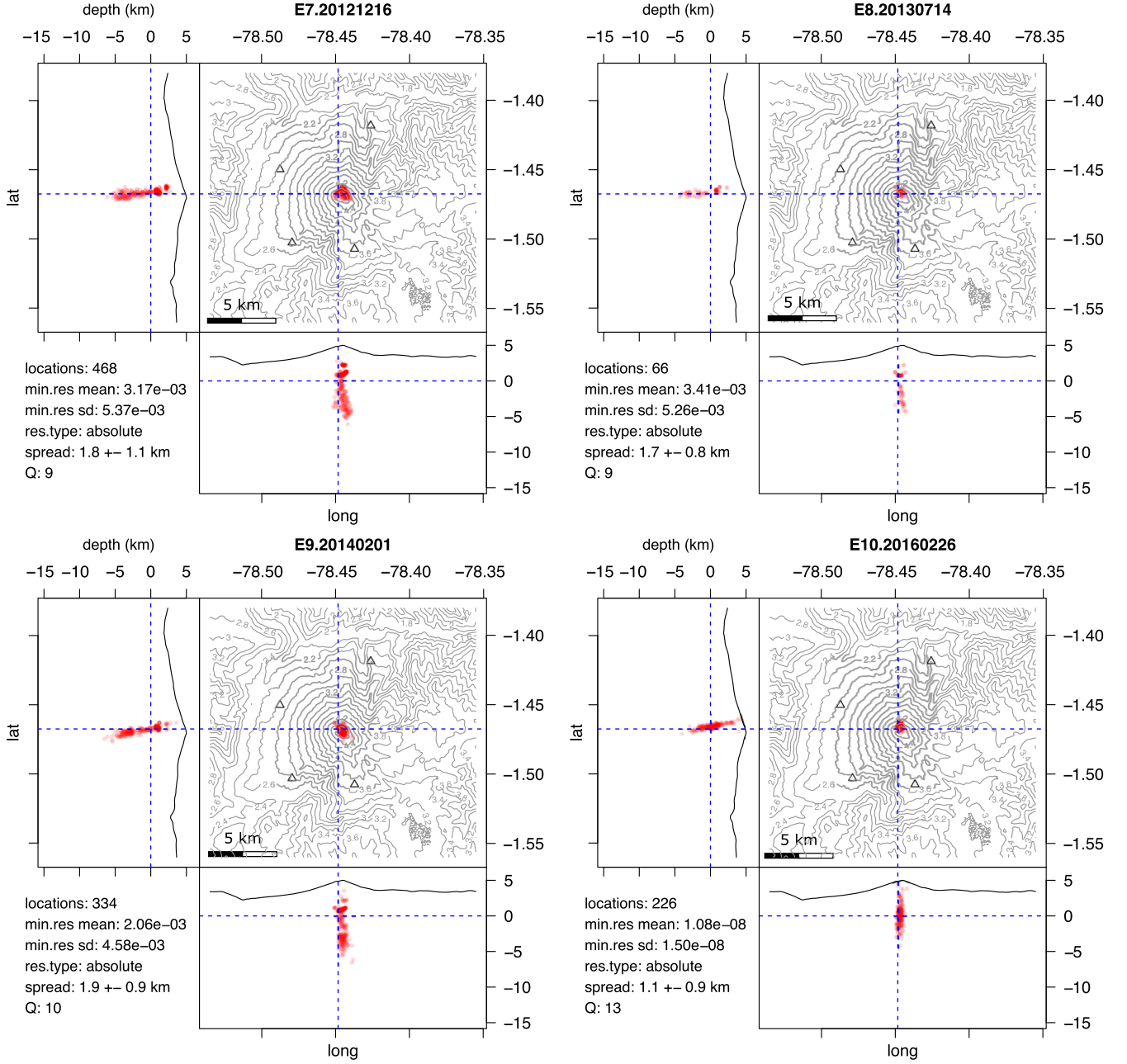


**Figure 15.** Locations of seismic sources of the paroxysms E7–E10. Blue dashed lines cross the volcanic vent and the sea level. The triangles represent the seismic stations used for the locations.

where we allow repeated terms in the central sums and emphasize the residual dependence with all station-source distances  $r_{ik}$ , being also the estimations  $\xi_{ik}$  distance-dependent functions,  $\xi_{ik} = \xi_{ik}(r_{ik})$ . The expression

$$\bar{\xi}_k = \frac{1}{n} \sum_{j=1}^n \xi_{jk}, \quad (18)$$

is the average of all the estimations for each source-node  $k$ .  $D_k$  and  $\Delta_k$  have the same optimal solution because they are only different by a constant, and this do not change the minimization condition, the null gradient. Similar argument can be set for the factor  $n$  in (17). Because of  $\partial \xi_{ik} / \partial r_{qk} = \delta_{iq} \partial \xi_{qk} / \partial r_{qk}$ , being  $\delta_{iq}$  the Kronecker's

delta, the residual gradient becomes

$$\frac{\partial \Delta_k}{\partial r_{qk}} = 2n \frac{\partial \xi_{qk}}{\partial r_{qk}} (\xi_{qk} - \bar{\xi}_k), \quad q = 1, \dots, n. \quad (19)$$

Consequently, the minimum condition  $\partial \Delta_k / \partial r_{qk} = 0$  is satisfied if each  $\partial \xi_{qk} / \partial r_{qk}$  is zero, or if each  $\xi_{qk}$  is equal to  $\bar{\xi}_k$ . The latter means that at the minimum residual location the estimations  $\xi_{qk}$  are close enough to be replaced by their average.

This demonstration supports the use of the eq. (18) as a theoretical approximation, approach used by some authors (Morioka *et al.* 2017; Walsh *et al.* 2017; Kumagai *et al.* 2019; Walsh *et al.* 2019), although they apply far-field approximations of velocity amplitude instead of our energy rate estimations. In general, the theoretical



**Table 3.** Parameter summary of paroxysm locations.

Ex	Locs	(−5, −3) km (%) <sup>(1)</sup>	(−1, 2) km (%) <sup>(1)</sup>	Q	Minimum residual mean (u) <sup>(2)</sup>	Centroid <sup>(3)</sup> (x, y, z) (km)	Spread (km)	Depths <sup>(4)</sup> (km)
E1	237	3.0	59.1	13	$2.3 \times 10^{-6}$	−0.02, 0.60, 1.06	1.6	−5.9, −4.1, 4.2
E2	860	1.9	59.7	14	$5.3 \times 10^{-7}$	0.08, 0.25, 1.18	1.5	−6.1, −3.8, 4.5
E3	234	5.6	62.0	15	$1.6 \times 10^{-8}$	−0.16, 0.78, 0.42	1.6	−7.1, −4.4, 4.0
E4	209	27.8	34.9	12	$1.5 \times 10^{-3}$	0.39, 0.09, −1.66	1.5	−5.0, −4.4, 2.6
E5	256	1.6	68.8	10	$9.0 \times 10^{-6}$	0.38, 0.35, 0.46	1.3	−4.3, −3.2, 4.1
E6	190	3.2	72.1	16	$3.7 \times 10^{-10}$	0.06, 0.37, 0.29	1.2	−3.8, −3.3, 4.3
E7	468	15.0	60.0	9	$3.2 \times 10^{-3}$	0.38, 0.10, −0.16	1.8	−6.1, −5.0, 2.8
E8	66	22.7	51.5	9	$3.4 \times 10^{-3}$	0.16, 0.12, −0.83	1.7	−4.4, −4.3, 2.2
E9	334	21.0	54.5	10	$2.1 \times 10^{-3}$	0.29, −0.05, −0.82	1.9	−6.5, −5.4, 3.6
E10	226	1.3	69.9	13	$1.1 \times 10^{-8}$	0.11, 0.23, 0.13	1.1	−4.1, −3.0, 4.3

<sup>(1)</sup>Percentage of locations either at the [−5, −3] or [−1, 2] km depth range.

<sup>(2)</sup>Residual units given by eq. (14):  $(\text{m}^5\text{s}^{-3}\text{Hz}^{-2})^2$ .

<sup>(3)</sup>Coordinates (x,y) relative to the vent (−78.4483, −1.4675) and z relative to the sea level.

<sup>(4)</sup>Minimum, quantile 1% and maximum location depth.

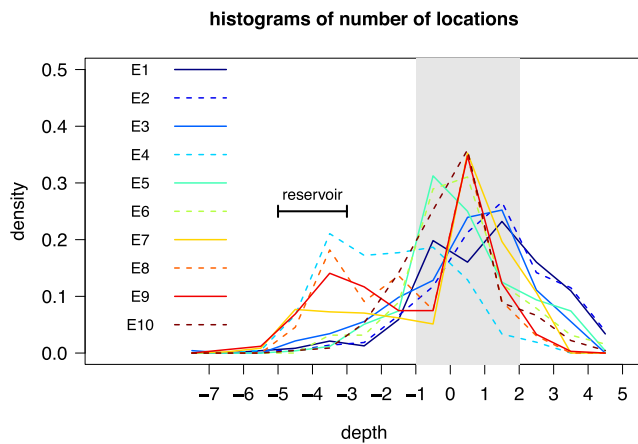


**Figure 16.** Density histograms of the number of locations for all the paroxysms, with 1 km width bins. The percentages of locations within the [−1, 2] km depth range, the grey interval, appear in the Table 3. Within the region between −5 and −3 km depth a reservoir might exist (Andújar et al. 2017, see our discussion section).

model, to be compared with the observations (or some transformation of them), is not necessarily the average of the observations, being common to use the observations to found the parameters that fit the best model (Legrand 2000). Eq. (17) demonstrates also that it is enough to compare the estimations between all the stations to get the same locations, instead of comparing the observations with the model given by the average (eq. 18).

At least absolute residuals and normalized residuals with a constant denominator are consistent with the eq. (18).

#### 4.3.2 The influence of normalized residual models

Several authors (Palacios et al. 2015; Ichihara & Matsumoto 2017; Morioka et al. 2017; Kumagai et al. 2019) use normalized residuals for seismic source location. These are values between 0 and 1, and are useful to compare the accuracy of two or more locations (e.g. Fig. 17). However, the residual plays also a key role in the source location, because such a location is identified with the minimum residual, being it a comparison process. Let us consider the following two normalized residual models:

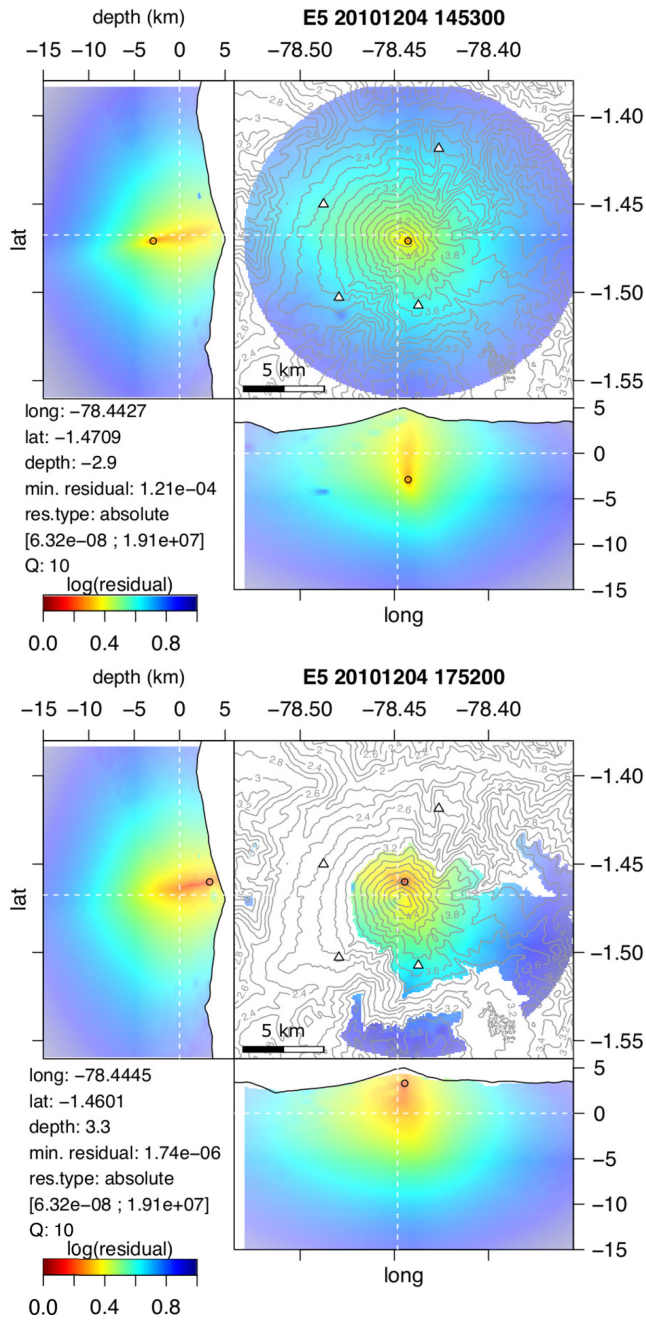
$$\Delta_k^{(1)} = \frac{2}{n(n-1)} \sum_{i>j} \frac{(\xi_{ik} - \xi_{jk})^2}{\xi_{ik}^2 + \xi_{jk}^2}, \quad (20)$$

$$\Delta_k^{(2)} = \frac{\sum_{i=1}^n (\xi_{ik} - \bar{\xi}_k)^2}{\sum_{i=1}^n \xi_{ik}^2} = 1 - \frac{n}{\sum_{i=1}^n (\xi_{ik} / \bar{\xi}_k)^2}, \quad (21)$$

And now suppose that we have three seismic stations and two source-nodes, with sets of estimation values {1, 2, 3} and {10, 20, 30}, respectively. The residual gets the same value for both sets because the scale factor between the sets is 10, and it is cancel out after applying either  $\Delta_k^{(1)}$  or  $\Delta_k^{(2)}$ . However, the absolute residual (eq. 17) of the second set is 100 times the residual of the first set. Hence, this two nodes are not equivalents, as the normalized residual values suggest. This case illustrates the main reason why we need a common denominator, a common gauge or scale, for the absolute residual, which is actually the measurement object. Normalizing it with a not dependent denominator on distances or travel times between the source and the stations, is equivalent to construct a measure system where the residual is its dimensionless part (Barenblatt 2003).

Fig. 20 presents the comparison between the locations using the residual model  $\Delta_k^{(2)}$ , and the absolute residual, for the paroxysm E3 with  $Q = 15$ . A similar result to panel (a) appears when the model  $\Delta_k^{(1)}$  is used. It is apparent that the locations with normalized residuals are more spread and deeper than those computed with the absolute residual. This effect is also observed in all the other paroxysms, E1–E10. The reason of this is because at deeper sources the normalizing denominators become larger, due to the far-field approximations are proportional to the source-station distances, thus causing decreasing of residual values and then being selected as the optimum minimum, instead of the absolute version. For this same reason, the residual map of a single location with the normalized residual models,  $\Delta_k^{(1)}$  or  $\Delta_k^{(2)}$ , use to have lower and spread values around the minimum, mainly going deeper, in comparison with locations based on absolute residuals (Fig. 21). Consequently, the lack of a good depth constraint in the locations is due to variable denominators within the normalized residuals.

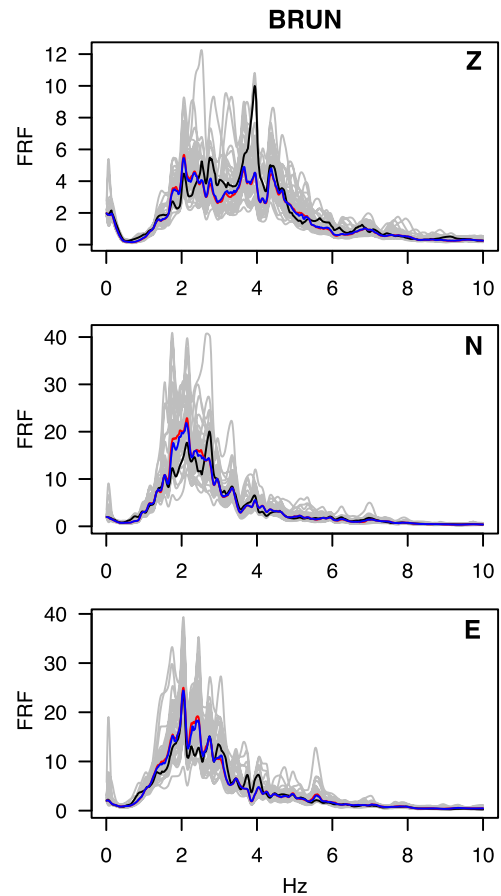
In addition, it is worthy to note that if the denominators change smoothly, depending on source-station distances or travel times, within a small region compared with the spatial dimensions of the seismic network, then, the locations may be similar to those found with absolute residuals, because the denominator would be close to a constant value, circumstance that should be verified. Similar situation occurs if the record window to be used is much longer than



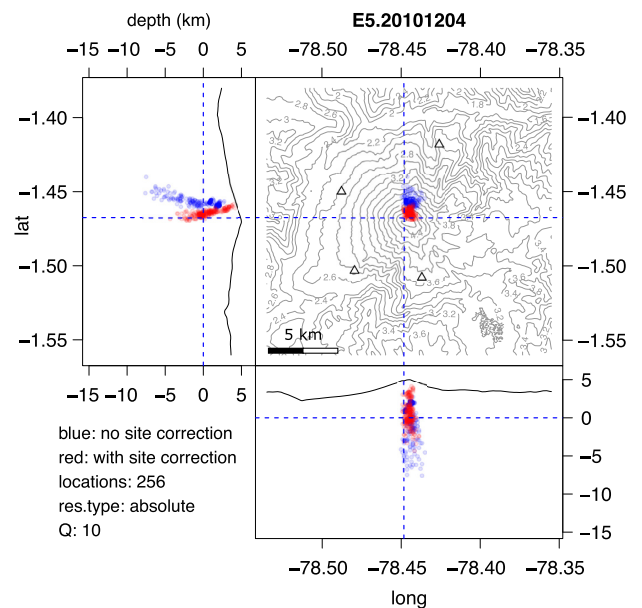
**Figure 17.** Comparison at the same colour scale of two absolute residual maps, of a deep (top panel) and a shallow (bottom panel) location of the paroxysm E5, with  $Q = 10$ . The common scale is defined with all the location residuals of the paroxysm.

arrival time differences for a given seismic network. We actually have selected this last criterion to cut records (creating 60 s moving windows) and to reduce the influence of the arrival time differences.

Studies by Battaglia (2003), Ichimura *et al.* (2018) and Walsh *et al.* (2020) are examples where the location residuals with constant denominators are used, because they are based only on observed values at the stations. However, two or more locations can not be compared because the observations change selecting a different data windows or event. If such comparison is needed a common scale, like that presented in Fig. 17, might be computed.



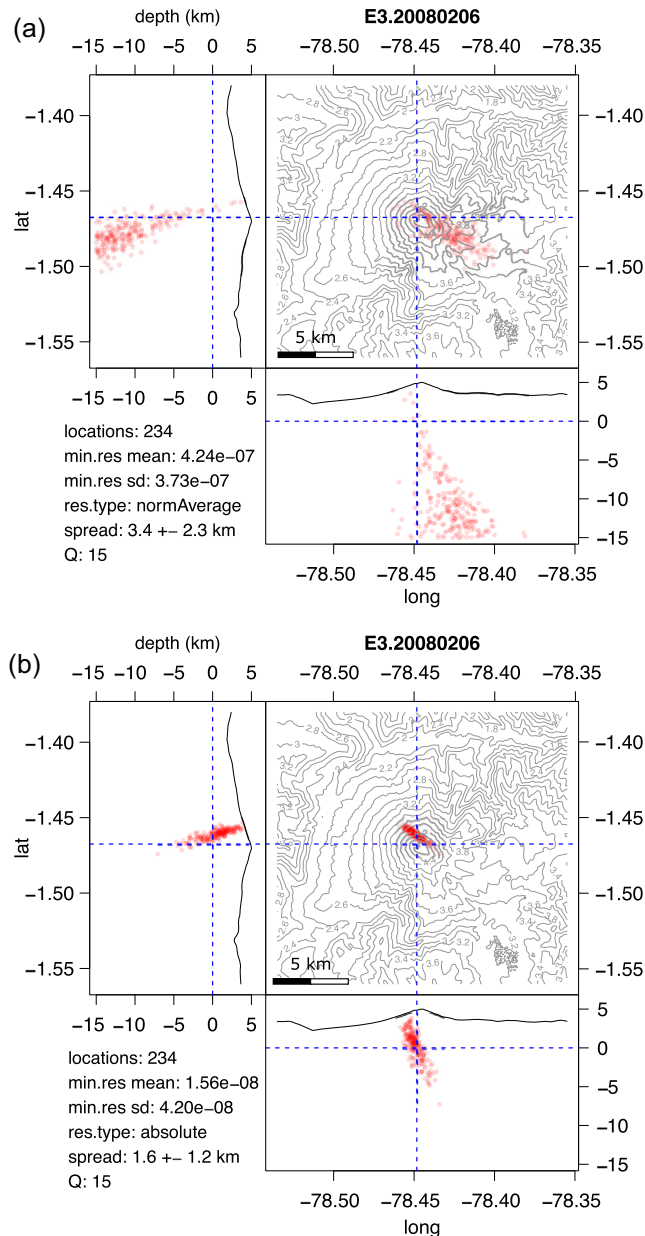
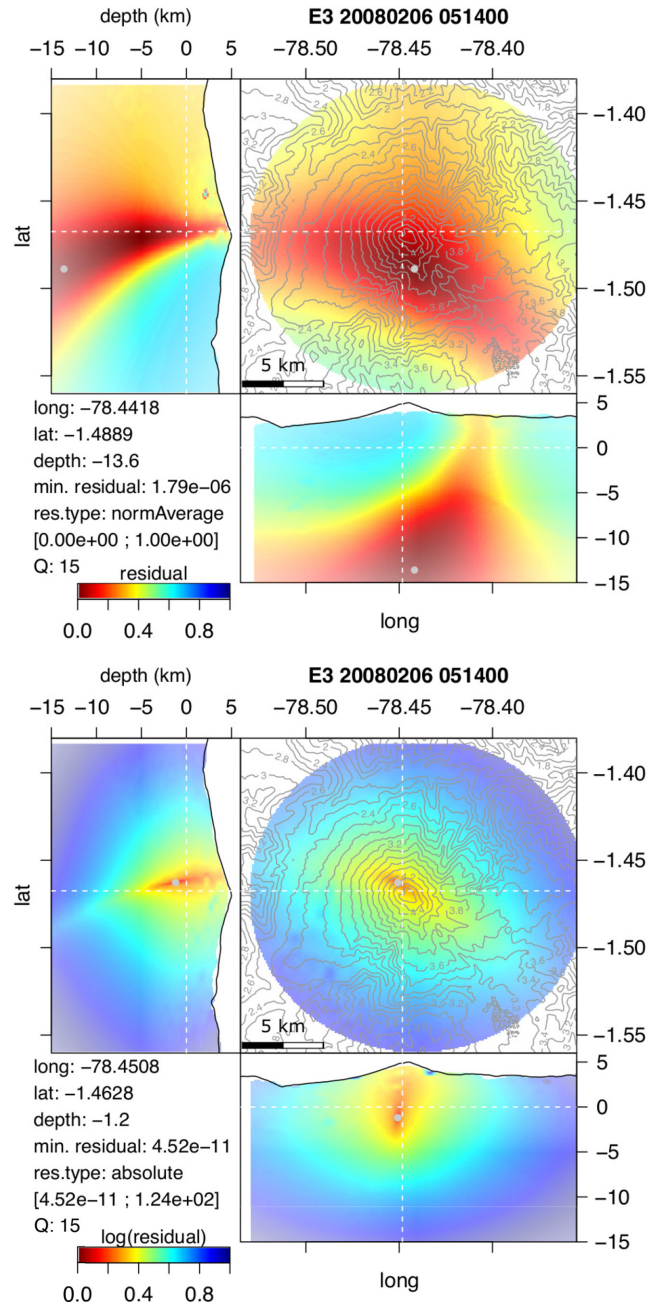
**Figure 18.** FRFs of BRUN computed with two different seismic networks to evaluate their dependence.



**Figure 19.** Locations of the paroxysm E5 from records not corrected (blue dots) and corrected (red dots) for site effects.

**Table 4.** Minimum-residual mean  $[(m^5 s^{-3} Hz^{-2})^2]$  of the paroxysm locations, from records corrected and not corrected for site effects.

Ex	Corrected	Not corrected
E1	$2.25 \times 10^{-6}$	$1.21 \times 10^{-4}$
E2	$5.26 \times 10^{-7}$	$6.90 \times 10^{-5}$
E3	$1.56 \times 10^{-8}$	$4.53 \times 10^{-6}$
E4	$1.50 \times 10^{-3}$	$2.41 \times 10^{+0}$
E5	$9.00 \times 10^{-6}$	$3.16 \times 10^{-3}$
E6	$3.69 \times 10^{-10}$	$4.19 \times 10^{-6}$
E7	$3.17 \times 10^{-3}$	$2.37 \times 10^{+0}$
E8	$3.41 \times 10^{-3}$	$6.18 \times 10^{+0}$
E9	$2.06 \times 10^{-3}$	$3.39 \times 10^{+0}$
E10	$1.08 \times 10^{-8}$	$4.89 \times 10^{-5}$

**Figure 20.** Locations of the paroxysm E3 with  $Q = 15$  using: panel (a) the normalized residual  $\Delta_k^{(2)}$  (eq. 21), and panel (b) the absolute residual (eq. 17). Blue dashed lines cross the volcanic vent and the sea level.**Figure 21.** Location and its residuals of a single 60-s window of the paroxysm E3, with  $Q = 15$ . Location computed with the residual model  $\Delta_k^{(2)}$  (top panel), and computed with the absolute residual, eq. (14), (bottom panel). White-dashed lines cross the volcanic vent and the sea level.

We conclude that better locations are possible to get applying absolute residuals or normalized residual models with a constant denominator.

#### 4.3.3 The paroxysm locations

The location of the paroxysmal tremors needs to tackle the volcanic heterogeneity, which is represented as a high variability of the seismic velocity field. Some approaches introduce random distributions in the velocity field to simulate the global effect of the heterogeneity (Sato 1977; Kumagai *et al.* 2011a). In these velocity fields, scatters within the volcanic edifice causes isotropic radiation



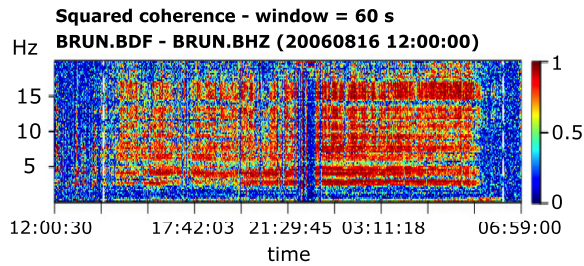


**Figure 22.** Ground-coupling airwaves of the paroxysm E2. The plot represents the squared coherence of infrasound (BDF) and vertical (BHZ) components for the 0–20 Hz range. Note that high coherence values are observed in the 5–10 Hz range.

patterns roughly in the range 5–10 Hz, similar to radiation patterns due to isotropic sources in a homogeneous medium, which is the property typically used in determining seismic locations. However, in our case, strong pyroclastic flows descending close to the stations and ground couplings of airwaves produce signals that overlap the 5–10-Hz frequency range (Fig. 22), which makes it impossible to locate internal seismic sources with this approach. For this reason, we present here a different procedure.

Considering the 10 paroxysms, we work in the range 0.4–2.5 Hz (Table 2). Analyses of regional earthquakes in Japan by Takemura *et al.* (2009) and simulations by Kumagai *et al.* (2011a) show weak interactions of seismic waves with the heterogeneities in the range 0.2–2 Hz, which in general overlaps with our intervals. Then, it is possible to omit the heterogeneities over a few hundreds of metres. This is encapsulated in the interpolation of the tomography, because the interpolation basically constructs a continuous and smooth velocity field with 100-m resolution. The disadvantage of this procedure is that the source radiation pattern could have a significant influence. However, we have assumed isotropic sources and acknowledge that further studies are necessary to consider other types of sources. Nevertheless, our locations show sources with well-constrained minimum residuals, suggesting that isotropic sources are an acceptable approximation here.

Kumagai *et al.* (2010) show significant influence of  $Q$  in the seismic source location. Then, they select the best  $Q$ , and an optimum frequency range, comparing them against the minimum residual (see their Fig. 9). For low  $Q$  values, they show also a decreasing behaviour of the residual while  $Q$  increases. This is exactly the same behaviour that we present in our Fig. 13. But in our case the residual is absolute, being actually the average of all minimum residuals of a group of locations, with a decreasing trend observed up to high  $Q$  values. What is certainly new in our observations is the finding that the locations become spatially closer, forming tighten clusters, while the  $Q$  value decreases. Tighten clusters is observed, for example, applying re-location methods based on waveform cross-correlations, where it is assumed that the waves were originated by the same seismic source. In this sense, locations forming tighten clusters combined with high residual values is then an unexpected result, and consequently an uncertainty effect arises: both the cluster spread and the cluster minimum-residual mean can not reach minima values simultaneously, when they are expressed as functions of  $Q$ . However, we select the best  $Q$  looking for the value that satisfies both criteria: tighten cluster and low residual. We have not yet a clear interpretation to explain why tighten clusters are generated with low  $Q$  values; further studies are needed. Our best  $Q$  values, for the 10 paroxysms, are between 9 and 16. These are values that may be expected for low frequencies in volcanic environments

(Jousset *et al.* 2004). Finally, notice that we use a fixed  $Q$  value for each paroxysm, as a global average for the entire volcano, however, it would be desirable in the future to determine a 3D map of this parameter for Tungurahua volcano.

Samaniego *et al.* (2011) and Andújar *et al.* (2017) studied the volcanic products of the 2006 paroxysms, E1 and E2. They found that the mineral composition of Tungurahua's andesitic magma (58–59 wt. percent  $\text{SiO}_2$ ) was formed at temperatures between 950 and 1025 °C and 200 and 400 MPa pressures, which suggests the existence of two reservoirs, one in the –5 to –3 km depth range (8–10 km below the summit – Fig. 16), and another in the –11- to –10 km depth range (15–16 km below the summit). The authors also suggest interactions between these two reservoirs before the eruptions. To confirm such a process, we would need to analyse in more detail the seismicity before and between these two eruptions. However, our evidence shows sparse locations between either –5.9 km (E1) or –6.1 km (E2), and –2 km depth (Figs 14 and 16, and Table 3). The major part of the locations start to concentrate at –2 km depth, roughly at the head of the shallow reservoir. This is consistent with the observed locations if we consider that, during the paroxysms, such locations should be related more to the path used by the magma, during its rising, than to the location where it is initially placed.

Although E1–E3 show sparse locations at the reservoir level, this situation changes with the paroxysms E4. This paroxysm started with a violent Vulcanian-type eruption that, almost immediately, produced pyroclastic flows without any increasing seismic activity. By contrast increasing seismic activity was typically observed during days before each one of the three previous paroxysms. It was also very different in terms of the ash composition, analysed by Bustillos (2010) who suggests that the onset may have been triggered by a phreatomagmatic interaction. However, our locations suggest a triggering process that could start at locations deeper than the usual depths of a hydrothermal system (Edwards *et al.* 2015; Zimanowski *et al.* 2015). We hypothesize that this paroxysm actually activated the region below the –1 km depth, because, after its occurrence, other Vulcanian paroxysms (E7–E9) show percentages of locations for that region larger than those of E1–E3. However, the activation mechanism remains unclear and needs further study. Hence, E4 may be the eruption responsible of the dynamics change in Tungurahua, defining a last period where Vulcanian eruptions arise more frequently. Actually, Hall *et al.* (2015), studying the pyroclastic flow deposits of E8 and E9, suggest that these Vulcanian eruptions are consequence of juvenile magma intrusions and cycles of plug formation-destruction in the upper part of the conduit.

In this paper, we present a new method for the determination and correction of site effects, and underline the importance of having infrasound sensors during the volcanic monitoring for a proper identification of the ground-coupled airwaves. We also propose the use of either absolute residuals or normalized residuals with constant denominators for locating sources, and to explore the influence of  $Q$  values in the analyses. Our locations clarify the dynamics change of Tungurahua volcano for the 2006–2016 eruptive sequence, relating the paroxysm E4 with the onset of a third and last eruptive period (2010–2016) dominated by the presence of Vulcanian eruptions.

## ACKNOWLEDGMENTS

This study has been possible thanks to the effort and support of Hiroyuki Kumagai through a JICA project in Ecuador between 2004



and 2009. This paper have been improved thanks to very useful comments of two anonymous reviewers. We appreciate the contribution of Indira Molina who shared the tomography data. Over the years of this study, we had useful discussions with Patricio Ramón, José Marrero and Pablo Samaniego. We thanks the technical assistance of Wilson Acero, Javier Pozo and Mercy Anchundia of systems and computational departments. Around two months of continuous processing was done with the HPC, the computational laboratory of MODEMAT (Mathematical Modelling Centre at the National Polytechnic School, Quito). This study was funded by SENESCYT (PhD studies at Bristol-UK, 2012–2016) and LMI (Laboratorio Mixto Internacional between IGEPN–Ecuador and IRD–France, 2016–2022). We thanks all the administrative support of Silvana Hidalgo, head of IGEPN, and its staff involved in the station maintaining.

## REFERENCES

- Aki, K., 1969. Analysis of the seismic coda of local earthquakes as scattered waves, *J. Geophys. Res.*, **74**(2), 615–631.
- Allard, J.F. & Atalla, N., 2009. *Propagation of Sound in Porous Media*, Wiley Ed.
- Anderson, J.F., Johnson, J.B., Steele, A.L., Ruiz, M.C. & Brand, B.D., 2018. Diverse eruptive activity revealed by acoustic and electromagnetic observations of the 14 July 2013 intense vulcanian eruption of Tungurahua volcano, Ecuador, *Geophys. Res. Lett.*, **45**(7), 2976–2985.
- Andújar, J., Martel, C., Pichavant, M., Samaniego, P., Scaillet, B. & Molina, I., 2017. Structure of the plumbing system at Tungurahua volcano, Ecuador: Insights from phase equilibrium experiments on July–August 2006 eruption products, *J. Petrology*, **58**(7), 1249–1278.
- Bablon, M., Quidelleur, X., Samaniego, P., Le-Pennec, J.-L., Lahitte, P., Liorzou, C., Bustillos, J.E. & Hidalgo, S., 2018. Eruptive chronology of Tungurahua volcano (Ecuador) revisited based on new K-Ar ages and geomorphological reconstructions, *J. Volcanol. Geotherm. Res.*, **357**, 378–398.
- Banks, H.T. & Joyner, M.L., 2017. AIC under the framework of least squares estimation, *Appl. Math. Lett.*, **74**, 33–45.
- Barenblatt, G.I., 2003. *Scaling*, Cambridge University Press. Cambridge Texts in Applied Mathematics.
- Battaglia, J., 2003. Location of seismic events and eruptive fissures on the Piton de la Fournaise volcano using seismic amplitudes, *J. Geophys. Res.*, **108**(B8), 2364.
- Battaglia, J., Hidalgo, S., Bernard, B., Steele, A., Arellano, S. & Acuña, K., 2019. Autopsy of an eruptive phase of Tungurahua Volcano (Ecuador) through coupling of seismo-acoustic and SO<sub>2</sub> recordings with ash characteristics, *Earth Planet. Sci. Lett.*, **511**, 223–323.
- Bell, A.F., Hernandez, S., Gaunt, H.E., Mothes, P., Ruiz, M., Sierra, D. & Aguaiza, S., 2017. The rise and fall of periodic ‘drumbeat’ seismicity at Tungurahua volcano, Ecuador, *Earth Planetary Sci. Lett.*, **475**, 58–70.
- Ben-Menahem, A. & Singh, S.J., 2000. *Seismic waves and sources*, Dover ed., 2nd edition.
- Boatwrite, J., 1980. A spectral theory for circular seismic sources; simple estimate of source dimension, dynamic stress drop, and radiated seismic energy, *Bull. Seismol. Soc. Am.*, **70**(1), 1–27.
- Boyd, S. & Vandenberghe, L., 2009. *Convex Optimization*, Cambridge University Press.
- Bustillos, J., 2010. Transición del estilo eruptivo durante las erupciones andesíticas en sistema abierto: contribuciones al estudio de los depósitos de ceniza del volán Tungurahua, *Prefalco, Dynamique des Systemes Geologiques et Aleas*, Université Nice, Sophia Antipolis, Tesis, Spanish.
- Butler, R., 2020. Bulk, shear and scattering attenuation beneath Hawaiian Volcanoes and in the oceanic crust extending to the Aloha Cabled Observatory, *Geophys. J. Int.*, **223**, 543–560.
- Buttkus, B., 2000. *Spectral Analysis and Filter Theory in Applied Geophysics*, Springer.
- Chapman, C., 2004. *Fundamentals of Seismic Wave Propagation*, Cambridge University Press.
- Campillo, M., Gariel, J.C., Aki, K. & Sánchez-Sesma, F.J., 1989. Destructive strong ground motion in Mexico City: Source, path, and site effects during great 1895 michoacan earthquake, *Bull. Seismol. Soc. Am.*, **79**(6), 1718–1735.
- Cannata, A., Montalto, P. & Patané, D., 2013. Joint analysis of infrasonic and seismic signals by cross wavelet transform: detection of Mt. Etna explosive activity, *Nat. Hazards Earth Syst. Sci.*, **13**, 1669–1677.
- Cruz-Atienza, V.M., Tago, J., Sanabria-Gómez, J.D., Chaljub, E., Etienne, V., Virieux, J. & Quintanar, L., 2016. Long duration of ground motion in the paradigmatic valley of Mexico, *Sci. Rep.*, **6**, 38807, doi:10.1038/srep38807.
- De la Cruz-Reyna, S., Tárraga, M., Ortiz, R. & Martínez-Bringas, A., 2010. Tectonic earthquakes triggering volcanic seismicity and eruptions. Case studies at Tungurahua and Popocatepetl volcanoes, *J. Volcanol. Geotherm. Res.*, **193**, 37–48.
- Edwards, B.R., Gudmundsson, M.T. & Russell, J.K., 2015. *Glaciovolcanism, in The Encyclopedia of Volcanoes*, Academic Press - Elsevier, 2nd Edition, Ed. H. Sigurdsson.
- Farsani, S.R., Ramian, A., Jarafi-Talookolaei, R.-A., Valvo, P.S. & Abedi, M., 2020. Free vibration analysis of rectangular sandwich plates with compressible core and various boundary conditions, *J. Sandw. Struct. Mater.*, 1–30, doi:10.1177/1099636220979276.
- Fee, D., Garces, M. & Steffke, A., 2010. Infrasonic from Tungurahua Volcano 2006–2008: Strombolian to Plinian eruptive activity, *J. Volcanol. Geotherm. Res.*, **193**, 67–81.
- Gaunt, H.E., Burgisser, A., Mothes, P.A., Browning, J., Meredith, P.G., Criollo, E. & Bernard, B., 2020. Triggering of the powerful 14 July 2013 Vulcanian eruption at Tungurahua Volcano, Ecuador, *J. Volcanol. Geotherm. Res.*, **392**, doi:10.1016/j.jvolgeores.2019.106762.
- Giordano, G. & De Astis, G., 2021. The summer 2019 basaltic Vulcanian eruptions (paroxysms) of Stromboli, *Bull. Volcanol.*, **83**, 1, doi:10.1007/s00445-020-01423-2.
- Hall, M.L., Robin, C., Beate, B., Mothes, P. & Monzier, M., 1999. Tungurahua Volcano, Ecuador: structure, eruptive history and hazards, *J. Volcanol. Geotherm. Res.*, **91**, 1–21.
- Hall, M.L., et al., 2015. Sequential plug formation, disintegration by Vulcanian explosions, and the generation of granular Pyroclastic Density Currents at Tungurahua volcano (2013–2014), Ecuador, *J. Volcanol. Geotherm. Res.*, **306**, 90–103.
- Ichihara, M. & Matsumoto, S., 2017. Relative source locations of continuous tremor before and after the subplinian events at shinmoe-dake, in 2011, *Geophys. Res. Lett.*, **44**, 10871–10877, doi:10.1002/2017GL075293.
- Ichihara, M., Yamakawa, K. & Muramatsu, D., 2021. A simple method to evaluate the air-to-ground coupling efficiency: a tool helping the assessment of seismic/infrasonic energy partitioning during an eruption, *Earth, Planets and Space*, **73**, 180, doi:10.1186/s40623-021-01510-4.
- Ichimura, M., Yokoo, A., Kagiya, T., Yoshikawa, S. & Inoue, H., 2018. Temporal variation in source location of continuous tremors before ash-gas emissions in January 2014 at Aso volcano, Japan, *Earth, Planets and Space*, **70**, 125, doi:10.1186/s40623-018-0895-4.
- IGEPN, 2008. Informe No. 5, Boletín Especial Volcán Tungurahua, IGEPN, Spanish – Special Official Report, (<https://www.igepn.edu.ec/tungurahua-a-informes/tung-especiales/tung-e-2008>, last access: 10 Jan 2023).
- IGEPN, 2016. Informe No. 836, Síntesis Semanal del Estado del Volcán Tungurahua, IGEPN–OVT, Spanish – Weekly Official Report.
- Johnson, J.B., Aster, R.C., Ruiz, M.C., Malone, S.D., McChesney, P.J., Lees, J.M. & Kyle, P.R., 2003. Interpretation and utility of infrasonic records from erupting volcanoes, *J. Volcanol. Geotherm. Res.*, **121**, 15–63.
- Jousset, P., Neuberg, J. & Jolly, A., 2004. Modelling low-frequency volcanic earthquakes in a viscoelastic medium with topography, *Geophys. J. Int.*, **159**, 776–802.
- Kato, K., Aki, K. & Takemura, M., 1995. Site amplification from coda waves: validation and application to S-wave site response, *Bull. Seismol. Soc. Am.*, **85**(2), 467–477.

- Kim, K., Lees, J.M. & Ruiz, M.C., 2014. Source mechanism of Vulcanian eruption at Tungurahua Volcano, Ecuador, derived from seismic moment tensor inversions, *J. Geophys. Res. Solid Earth*, **119**, doi:10.1002/2013JB010590.
- Kot, M., 2014. A first course in the calculus of variations, *AMS, Am. Math. Soc.*, Student Mathematical Library, 72, ISBN 978-1-4704-1495-5.
- Kumagai, H., *et al.*, 2007. Enhancing volcano-monitoring capabilities in Ecuador, *EOS, Trans. Am. Geophys. Union*, **88**(23), 245–252.
- Kumagai, H., *et al.*, 2010. Broadband seismic monitoring of active volcanoes using deterministic and stochastic approaches, *J. Geophys. Res.*, **115**, B08303, doi:10.1029/2009JB006889.
- Kumagai, H., Saito, T., O'Brien, G. & Yamashina, T., 2011a. Characterization of scattered seismic wavefields simulated in heterogeneous media with topography, *J. Geophys. Res.*, **116**, B03308, doi:10.1029/2010JB007718.
- Kumagai, H., Palacios, P., Ruiz, M., Yepes, H. & Kozono, T., 2011b. Ascending seismic source during an explosive eruption at Tungurahua volcano, Ecuador, *Geophys. Res. Lett.*, **38**, L01306, doi:10.1029/2010GL045944.
- Kumagai, H., Mothes, P., Ruiz, M. & Maeda, Y., 2015. An approach to source characterization of tremor signals associated with eruptions and lahars, *Earth, Planets and Space*, **67**, 178, doi:10.1186/s40623-015-0349-1.
- Kumagai, H., Londoño, J.M., Maeda, Y. & Acevedo, A.E., 2019. Amplitude source location method with depth-dependent scattering and attenuation structures: application at Nevado del Ruiz Volcano, Colombia, *J. Geophys. Res.: Solid Earth*, **124**, 11585–11600, doi:10.1029/2019JB018156.
- Légrand, D., Kaneshima, S. & Kawakatsu, H., 2000. Moment tensor analysis of near-field broadband waveforms observed at Aso Volcano, Japan, *J. Volcanol. Geotherm. Res.*, **101**, 155–169.
- Le Pennec, J., *et al.*, 2005. Los peligros volcánicos asociados con el volcán Tungurahua, Corporación Editora Nacional, 2nd ed., IRD–IGEPN, ISBN 9978-84-402-3, Spanish.
- Le Pennec, J.-L., Jaya, D., Samaniego, P., Ramón, P., Moreno Yáñez, S., Egred, J. & van der Plicht, J., 2008. The AD 1300–1700 eruptive periods at Tungurahua volcano, Ecuador, revealed by historical narratives, stratigraphy and radiocarbon dating, *J. Volcanol. Geotherm. Res.*, **176**, 70–81.
- Madariaga, R., 2015. Seismic source theory. In *Treatise on Geophysics*, Second Edition, *Elsevier*, **4**, 51–71.
- Matoza, R. & Fee, D., 2014. Infrasonic component of volcano-seismic eruption tremor, *Geophys. Res. Lett.*, **41**, 1964–1970.
- Matoza, R. & Fee, D., 2018. The inaudible rumble of volcanic eruptions, *Acoustics Today*, **14**(1), 17–25.
- Mayeda, K., Koyanagi, S. & Aki, K., 1991. Site amplification from S-wave coda in the long valley caldera region, California, *Bull. Seismol. Soc. Am.*, **81**(6), 2194–2213.
- McKee, K., David, F., Haney, M., Matoza, R.S. & Lyons, J., 2018. Infrasound Signal Detection and Back Azimuth Estimation Using Ground-Coupled Airwaves on Seismo-Acoustic Sensor Pair, *J. Geophys. Res., Solid Earth*, **123**, 6826–6844.
- Molina, I., 2001. Actividad pre-eruptiva del volcán tungurahua, *Tesis: Universidad de Caldas*, Facultad de Ciencias Exactas y Naturales, Programa de Geología y Minas, Manizales - Colombia, Instituto Geofísico, EPN, Quito - Ecuador. Spanish.
- Molina, I., Kumagai, H., Le Pennec, J.-L. & Hall, M., 2005. Three-dimensional P-wave velocity structure of tungurahua volcano, Ecuador, *J. Volcanol. Geotherm. Res.*, **147**, 144–156.
- Montero, J.-M. & Fernández-Avilés, G., 2015. Spatial and spatio-temporal geostatistical modeling and kriging, John Wiley & Sons, Ltd.
- Morioka, H., Kumagai, H. & Maeda, T., 2017. Theoretical basis of the amplitude source location method for volcano-seismic signals, *J. Geophys. Res.*, **122**, doi:10.1002/2017JB013997.
- Palacios, P., Kendall, J.-M. & Mader, H., 2015. Site effect determination using seismic noise from Tungurahua volcano (Ecuador): implications for seismo-acoustic analysis, *Geophys. J. Int.*, **201**, 1082–1098.
- Palacios, P.B., Díez, M., Kendall, J.-M. & Mader, H.M., 2016. Seismic-acoustic energy partitioning during a paroxysmal eruptive phase of Tungurahua volcano, Ecuador, *Geophys. J. Int.*, **205**, 1900–1915.
- Pappalardo, L., D'Auria, L., Cavallo, A. & Fiore, S., 2014. Petrological and seismic precursors of the paroxysmal phase of the last Vesuvius eruption on March 1944, *Nat. Sci. Rep.*, **4**, 6297, doi:10.1038/srep06297.
- R Core Team, 2022. R: A language and environment for statistical computing, *R Foundation for Statistical Computing*, Vienna.
- Safak, E., 1995. Discrete-time analysis of seismic site amplification, *J. Eng. Mech.*, **121**, 801–809.
- Samaniego, P., Le Pennec, J.-L., Robin, C. & Hidalgo, S., 2011. Petrological analysis of the pre-eruptive magmatic process prior to the 2006 explosive eruptions at Tungurahua volcano (Ecuador), *J. Volcanol. Geotherm. Res.*, **199**, 69–84.
- Sato, H., 1977. Energy propagation including scattering effects single isotropic scattering approximation, *J. Phys. Earth.*, **25**, 27–41.
- Sato, H., Fehler, M.C. & Maeda, T., 2012. *Seismic Wave Propagation and Scattering in Heterogeneous Earth*, 2nd ed., Springer, ISBN 978-3-642-23028-8.
- Sciotto, M., Cannata, A., Di Grazia, G., Gresta, S., Privitera, E. & Spina, L., 2011. Seismoacoustic investigations of paroxysmal activity at Mt. Etna volcano: New insights into the 16 November 2006 eruption, *J. Geophys. Res.*, **116**, B09301, doi:10.1029/2010JB008138.
- Semblat, J.F., Kham, M., Parara, E., Bard, P.Y., Pitilakis, K., Makra, K. & Raptakis, D., 2005. Seismic wave amplification: Basin geometry vs soil layering, *Soil Dyn. Earthq. Eng.*, **25**, 529–538.
- Stein, S. & Wysession, M., 2003. *An Introduction to Seismology, Earthquakes and Earth Structure*, Blackwell Publishing.
- Takemura, S., Furumura, T. & Saito, T., 2009. Distortion of the apparent S-wave radiation pattern in the high-frequency wavefield: Tottori-Ken Seibu, Japan, earthquake of 2000, *Geophys. J. Int.*, **178**, 950–961.
- Walsh, B., Jolly, A.D. & Procter, J., 2017. Calibrating the amplitude source location (ASL) method by using active seismic sources: An example from Te Maari volcano, Tongariro National Park, New Zealand, *Geophys. Res. Lett.*, **44**, 3591–3599.
- Walsh, B., Procter, J., Lokmer, I., Thun, J., Hurst, T. & Christenson, B., 2019. Geophysical examination of the 27 April 2016 Whakaari/White Island, New Zealand, eruption and its implications for vent physiognomies and eruptive dynamics, *Earth, Planets and Space*, **71**, 25, doi:10.1186/s40623-019-1003-0.
- Walsh, B., Procter, J. & Jolly, A., 2020. Improving the amplitude source location (ASL) method using multicomponent seismic data: an assessment with active source seismic data, *Bull. Seismol. Soc. Am.*, **110**(1), doi:10.1785/0120190063.
- Yoshida, N., 2015. *Seismic Ground Response Analysis*, Springer, Geotechnical, Geological and Earthquake Engineering, **36**, doi:10.1007/978-94-017-9460-2.
- Zimanowski, B., Buttner, R., Dellino, P., White, J.D.L. & Wohletz, K.H., 2015. Magma–Water Interaction and Phreatomagmatic Fragmentation, in *The Encyclopedia of Volcanoes*, Academic Press - Elsevier, 2nd Edition, Ed. H. Sigurdsson.

## APPENDIX A: EARTHQUAKES USED FOR THE SITE EFFECT DETERMINATION

The earthquake parameters used to compute the site FRFs are presented in Table A1.

**Table A1.** Earthquake parameters.

EQ	Origing time	Longitude <sup>(1)</sup>	Latitude	Absolute depths <sup>(2)</sup> (km)	Magnitude	Type	Distance <sup>(3)</sup> (km)	End time <sup>(4)</sup> (s)
EQ01	20060728 07:18:45.30	−76.9850	0.6830	3.3	4.0	Md	289.0	184.68
EQ02	20060805 10:21:20.70	−78.1500	−2.6930	12.0	3.7	Md	140.1	99.28
EQ03	20060806 05:33:02.98	−80.3180	−3.0680	51.1	4.6	mb	273.5	197.00
EQ04	20060809 13:54:10.53	−80.3920	−1.7530	12.0	4.0	Md	218.3	119.45
EQ05	20060816 05:16:20.40	−78.1220	−1.7210	12.0	4.3	mb	45.9	74.58
EQ06	20110722 08:20:38.44	−80.0715	−1.6495	0.0	4.2	MLv	181.5	121.54
EQ07	20110726 20:58:30.20	−76.9563	−2.8073	124.15	4.9	MLv	222.8	139.78
EQ08	20110818 05:23:46.35	−80.2267	−3.0359	50.39	4.7	MLv	263.5	163.63
EQ09	20110902 03:46:08.54	−79.9299	−3.5390	73.33	5.2	MLv	283.0	131.44
EQ10	20111114 02:21:48.80	−79.3882	−2.7970	5.80	4.1	MLv	180.9	141.19
EQ11	20111230 07:12:59.12	−79.0766	−2.2480	119.45	4.2	MLv	111.3	120.86
EQ12	20120110 18:07:09.07	−80.4505	−0.8328	4.84	4.9	MLv	233.4	170.91
EQ13	20120208 10:54:41.95	−79.3135	0.6240	4.84	5.7	MLv	251.5	138.03
EQ14	20120429 00:43:22.36	−79.8524	−2.3892	49.46	4.9	MLv	186.6	137.62
EQ15	20120429 23:42:31.01	−79.7291	−2.0871	25.88	4.2	MLv	158.1	108.97
EQ16	20120730 05:19:44.12	−80.7770	−1.9446	10.00	5.3	MLv	264.1	155.86
EQ17	20120809 10:52:00.58	−77.4048	−1.9292	12.00	4.3	MLv	126.8	79.40
EQ18	20130117 13:12:41.20	−80.8346	−1.1109	10.00	4.7	MLv	268.1	158.78
EQ19	20130224 08:59:59.10	−78.9669	0.9719	12.00	4.6	MLv	277.1	160.88
EQ20	20130227 15:56:09.03	−79.0425	−3.5549	112.06	5.0	MLv	241.1	150.95
EQ21	20130326 02:58:56.57	−77.2906	−2.1450	12.00	4.0	MLv	149.0	73.41
EQ22	20130403 08:13:47.94	−80.2998	−1.8846	17.61	4.3	MLv	210.9	132.04
EQ23	20130410 00:52:46.80	−79.8112	−2.2121	79.00	5.0	MLv	172.6	113.18
EQ24	20130427 11:18:40.61	−79.3091	−3.0991	37.37	4.1	MLv	205.0	119.37
EQ25	20130429 02:32:50.28	−78.8808	−3.3508	80.30	5.0	MLv	214.7	149.70
EQ26	20130512 13:14:31.09	−77.9672	−3.4671	30.63	4.8	MLv	228.5	108.89
EQ27	20130529 05:46:30.76	−79.1564	0.6683	5.00	4.0	MLv	250.0	129.25
EQ28	20130618 06:43:06.28	−70.1026	−3.8594	77.50	4.5	MLv	275.5	133.70
EQ29	20130626 10:51:28.30	−80.6570	−2.8760	16.18	5.0	MLv	291.1	161.68
EQ30	20130701 06:01:29.60	−80.6317	−0.8195	20.42	4.3	MLv	253.1	150.38
EQ31	20130914 17:00:08.98	−79.0746	−2.2288	84.80	4.5	MLv	109.5	101.00
EQ32	20130917 23:03:53.57	−77.1766	−2.4857	24.00	4.8	MLv	181.0	86.41
EQ33	20131001 10:45:26.35	−79.7471	−2.2866	30.11	4.7	MLv	170.6	93.63
EQ34	20131101 07:30:04.97	−80.0471	0.2927	8.00	5.0	MLv	264.2	135.01
EQ35	20131128 03:24:03.29	−80.4246	−1.6856	8.00	4.4	MLv	220.9	106.69
EQ36	20131130 16:38:53.23	−77.2369	−2.6777	21.72	5.5	MLv	190.3	96.75
EQ37	20131220 10:37:37.60	−77.5532	−2.9498	10.00	4.3	MLv	192.4	92.38
EQ38	20140309 02:10:57.80	−77.6525	0.5206	8.00	4.3	MLv	239.2	142.19
EQ38	20140314 20:53:54.88	−79.8715	−2.0914	52.00	5.5	MLv	83.8	95.10
EQ40	20140430 05:43:06.48	−77.9094	0.7833	10.00	4.7	MLv	257.2	223.50
EQ41	20140812 19:57:58.00	−78.4109	−0.0618	5.00	5.0	MLv	156.2	201.98

<sup>(1)</sup>WGS84 longitude–latitude coordinate system. <sup>(2)</sup>Absolute depths: relative to the sea level, downward is positive.

<sup>(3)</sup>Epicentral distance relative to the volcanic vent. <sup>(4)</sup>Seconds after the origin time when the earthquake window ends.

## APPENDIX B: MINIMUM DISTANCE BETWEEN REFERENCE LEVEL VECTORS

In Fig. 3, the change of the reference level vector  $\mathbf{l}_k^0$  to  $\mathbf{l}_k^\delta$  by a small increase  $\delta f$  in the frequency, from  $f_0$  to  $f_0 + \delta f$ , produces a non-parallel case, with a  $2\theta$  angular difference. We look for the bisectrix as a hiperplane within the  $n$ -dimensional space  $\Lambda$  that crosses the origin of the coordinate system. To prove that such a plane exists let  $\hat{\mathbf{u}}^o$  and  $\hat{\mathbf{u}}^\delta$  be unit vectors along  $\mathbf{l}_k^0$  and  $\mathbf{l}_k^\delta$ , respectively, and let  $\hat{\mathbf{a}}$  be the unit vector perpendicular to the plane. Then, the sum  $\hat{\mathbf{u}}^o + \hat{\mathbf{u}}^\delta$  is parallel and within the bisectrix, while the difference  $\hat{\mathbf{u}}^o - \hat{\mathbf{u}}^\delta$  is perpendicular to it, because the scalar product

$(\hat{\mathbf{u}}^o + \hat{\mathbf{u}}^\delta) \cdot (\hat{\mathbf{u}}^o - \hat{\mathbf{u}}^\delta) = 0$ . Hence, the unit vector that defines the plane is

$$\hat{\mathbf{a}} = \frac{\hat{\mathbf{u}}^o - \hat{\mathbf{u}}^\delta}{|\hat{\mathbf{u}}^o - \hat{\mathbf{u}}^\delta|}, \quad (\text{B1})$$

which is possible only if  $\mathbf{l}_k^0$  and  $\mathbf{l}_k^\delta$  are not parallel. This plane is unique because, if a second bisectrix with normal vector  $\hat{\mathbf{a}}'$  exists, the sum  $\hat{\mathbf{u}}^o + \hat{\mathbf{u}}^\delta$  must be parallel and within it, satisfying that  $(\hat{\mathbf{a}} - \hat{\mathbf{a}}') \cdot (\hat{\mathbf{u}}^o + \hat{\mathbf{u}}^\delta) = 0$ , which is possible only if  $\hat{\mathbf{a}}' = \hat{\mathbf{a}}$ , for arbitrary vectors  $\hat{\mathbf{u}}^o$  and  $\hat{\mathbf{u}}^\delta$ .

Thus, Fig. 3 represents the two-dimensional cross-section perpendicular to the bisectrix that contains the vectors  $\mathbf{l}_k^0$  and  $\mathbf{l}_k^\delta$ , and where the segments that define the distance between them are included.



The distance is defined as the sum of three positive terms,  $\mathcal{D} = AD + CD + CB$  and its value changes when either the point B or C moves. Let  $OC = x$ , then  $\mathcal{D}(x) = AD + |OD - x| + x \tan(\theta)$ , with  $x > 0$ . Because its derivative is

$$\frac{\partial \mathcal{D}}{\partial x} = -\text{Sgn}(OD - x) + \tan(\theta) = \begin{cases} -1 + \tan(\theta) & x < OD \\ 1 + \tan(\theta) & x > OD, \end{cases} \quad (\text{B2})$$

where  $\text{Sgn}(z)$  is the sign function,  $\mathcal{D}(x)$  reaches a minimum at  $x = OD$ , which implies  $CD = 0$ . Hence, to have the minimum it is needed  $\tan(\theta) < 1$ , that is,  $0 < \theta < \pi/4$ , which satisfies the constraint that all reference levels must be positive. Furthermore, because of the assumed continuity of the FRF, a small change  $\delta f$  will cause a small  $\theta$ .

## APPENDIX C: RESIDUAL OPTIMIZATION

First, we shall prove that the function  $\Delta_k(f)$  is convex. It guaranties that any local optimum is a minimum (Boyd & Vandenberghe 2009). Writing the function in the form (omitting the component index  $k$ )

$$\Delta(I) = \Delta(L_1, \dots, L_n) = \sum_i \sum_j (L_i \tau_i - L_j \tau_j)^2, \quad (\text{C1})$$

it is enough to prove that

$$\Delta(\beta I) + \Delta((1 - \beta)I') \leq \beta \Delta(I) + (1 - \beta) \Delta(I'), \quad (\text{C2})$$

for any pair  $I, I'$  and any  $\beta \in [0, 1]$ , to ensure that the function is convex. Indeed it occurs because

$$\Delta(\beta I) + \Delta((1 - \beta)I') = \beta^2 \Delta(I) + (1 - \beta)^2 \Delta(I'), \quad (\text{C3})$$

and both  $\beta^2 \leq \beta$  and  $(1 - \beta)^2 \leq (1 - \beta)$ , for  $\beta$  between 0 and 1. Then, because  $\Delta(I) \geq 0$ , the null vector is a global minimum and the function is convex.

To find the reference levels  $l_i = \sqrt{L_i}$ , for the  $n$  stations, the following constraints are added:

$$\sum_i L_i = L_0, \quad \text{with} \quad L_i > 0. \quad (\text{C4})$$

Around of the local minimum each term of the sum in  $\Delta(I)$  should be small enough to ensure that  $\tau_i/\tau_j \approx L_j/L_i$ . Due to  $\tau_i$  and  $\tau_j$  are positive,  $L_i$  and  $L_j$  have always the same sign; and because  $\sum_i L_i = L_0 > 0$ , all  $L_i$  must be positive. This result permits to relax the number of constraints to one, writing the Lagrangian as eq. (9) shows. Because of the convexity of  $\Delta(I)$  and the given constraint, the local minimum exists and is unique, it is not the global minimum

because  $L_0 > 0$ , and therefore, the matrix  $\mathbb{T}^{-1}$  of the linear system (10) exists, giving the solution:

$$\mathbb{L} = \mathbb{T}^{-1} \mathbb{L}_0. \quad (\text{C5})$$

## APPENDIX D: DENSE ARRAYS OF VELOCITIES, PATH LENGTHS AND TRAVEL TIMES

The Ordinary Kriging (OK) interpolation method (Montero & Fernández-Avilés 2015) is usually supervised, which implies a manual selection of the semivariogram model that best fit the data before any interpolation. However, this process is here automatised with the following procedure.

If it is given some information  $Z_k$  (either velocities, ray path lengths or travel times),  $k = 1, 2, \dots, n$ , for a grid of  $n$  nodes, with coordinates  $n_k = (x_k, y_k, z_k)$ , and an arbitrary point  $s = (s_x, s_y, s_z)$  where the interpolation  $Z_s$  is needed, then, if  $s$  is very close, less than 50 m to some node  $k$ , the interpolatizon is  $Z_s = Z_k$  (due to the limit property of OK). Otherwise, all the neighbours within the 3 km width cube, centred around the point  $s$ , are selected ( $\sim 343$  nodes) and the empirical semivariogram is computed, which is constructed with 10 bins. The semivariogram models: Spherical, Cubic, Stable and Cauchy (Montero & Fernández-Avilés 2015) are fitted with the 'optim' function (R Core Team 2022). Then, the best model is selected with the Akaike Information Criterion (Banks & Joyner 2017),  $\text{AIC} = 2q + m \ln(R)$ , where  $q$  is the number of parameters,  $m$  the number of observations and  $R$  the sum of the squared residuals. Finally, the interpolation is computed with the selected semivariogram following the usual procedure for OK.

Two key aspect must be taken into account in the ray path length and travel time computation for each node-station pair, which is achieved applying the Fermat's principle. First, this principle implies an optimization procedure, which requires to know the velocity field information at any point and not only at the node locations. This is the reason why the velocity information is first interpolated to 100-m node spacing, for then to apply the inverse distance method for an arbitrary point. The inverse distance method uses the neighbours located up to 100 m from the desired point ( $\sim 8$  nodes). Secondly, to get paths lengths and travel times from the denser 100-m node spacing grid demands high computational resources, because of the number of nodes. However, computing them from the 500-m node spacing grid and then interpolating the information to 100-m node spacing, is much faster because the number of nodes is two orders less than the denser grid.